Subsurface Vapor-Phase Transport of TCA at MDA L: Model Predictions

Philip Stauffer

Kay Birdsell

Marc Witkowski

Terry Cherry

and

John Hopkins

Earth and Environmental Sciences Division
Los Alamos National Laboratory

April, 2000

8978

Table of Contents

1.0 Introduction 4

2.0 Site Description 6
- 2.1 Stratigraphy and topography 6
- 2.2 Contaminant source 8
  - 2.2.1 Timing of waste disposal at MDA L 8
  - 2.2.2 Types of waste found at MDA L 9
  - 2.2.3 Pore-gas monitoring data 11
- 2.3 Conceptual model and Model assumptions 12
  - 2.3.1 Unsaturated-zone transport processes 12
  - 2.3.2 The effect of system geometry on plume growth 13
  - 2.3.3 Release and mobility of TCA vapor 13
- 2.4 Hydrogeologic data 14
- 2.5 Transport properties 15

3.0 Numerical Model of TCA Transport at MDA L 16
- 3.1 Model domain and computational grid 16
- 3.2 Boundary and initial conditions 18
- 3.3 Shafts and asphalt 19
- 3.4 Summary of the logic flow for the base simulation 20

4.0 Results 21
- 4.1 Base simulation results 21
  - 4.1.1 TCA concentrations through the model domain 21
  - 4.1.2 Surface flux 22
  - 4.1.3 Goodness of fit of the base simulation 25
- 4.2 Model behavior with variation from the base simulation 26
- 4.3 Results from the best-fit simulation 28
  - 4.3.1 Basic results 28
  - 4.3.2 Current plume growth 34
  - 4.3.3 Future plume growth: Year 2000 to 2050 35
  - 4.3.4 Simulating catastrophic drum failure with the best-fit simulation 36
- 4.4 Future work 38

5.0 Conclusions 39

6.0 Acknowledgements 41

7.0 References 42

List of Figures and Tables

Figure Number

2.1_1	Geographical information for MDA L and the surrounding area.	7
2.1_2	Simplified site stratigraphy.	8
2.2_1	Location map for waste disposal shafts and pits at MDA L.	9
2.2_2	Second quarter FY99, MDA L, TCA concentration data contoured on a plane 18 m (60 ft.) below the mesa top.	11
3.1_1	Model topography and computational grid.	17
3.1_2	Model stratigraphy for cross-section B-B'.	18
4.1.1_1	TCA concentration for the base simulation contoured on a plane 18 m below the mesa top.	21
4.1.1_2	TCA concentration for the data versus the base simulation on a plane 49 m below the mesa top.	23
4.1.2_1	Flux of TCA to the atmosphere for the base simulation.	24
4.2_1	Regression plots for simulations presented, based on GOF statistics.	28
4.2_2	Regression plot for simulations presented, based on removing potentially spurious data.	29
4.3.1_1	The effect of fixing the basalt and the north and west boundaries to zero concentration on the concentrations deep in the model domain.	30
4.3.1_2	Vertical slice through the best-fit simulation at cross-section B-B′.	31
4.3.1_3	Vertical slice through the best-fit simulation at cross-section C-C′.	32
4.3.1_4	Amount of TCA in the subsurface as a function of time.	33
4.3.1_5	Amount of TCA injected and produced as a function of time.	33
4.3.2_1	Best-fit simulation, change in concentration with time at five locations.	34
4.3.3_1	Best-fit simulation, future plume growth.	35
4.3.4_1	Comparison of no drum failure simulation with drum failure simulation.	37
4.3.4_2	Time dependence of TCA removal from the mesa after catastrophic drum failure.	38

Table Number

1	Physical parameters used in the numerical model.	14
2	Goodness of fit statistics for simulations presented.	26

1.0 - INTRODUCTION

TA-54 MDA L is a material disposal area (MDA) that received mixed liquid wastes (hazardous and radioactive components) from the late 1950's through 1986 [LANL, 2000]. From the late 1950's through 1975, bulk liquid waste was disposed of in an open pit at MDA L and allowed to evaporate. Due to the high vapor pressure of the organic liquids, most of the VOCs introduced to the open pit should have readily evaporated into the atmosphere. From 1975 through 1985, organic liquids were disposed of in a series of 20-m deep shafts. Some organic liquids were poured directly into the shafts while others were containerized in drums before being disposed of in the shafts. All of these disposal operations occurred beneath the surface of Mesita del Buey in the underlying unsaturated tuff units, some 300 meters above the regional aquifer.

The major chemicals of potential concern (COPC) measured at this site are found in pore-gas sampling and include a host of volatile organic compounds (VOCs) and tritium [LANL, 2000]. Although VOCs may percolate as liquids in the subsurface (especially in saturated systems) the dry subsurface environment at MDA L causes rapid volatilization. In fact, core sampling has failed to reveal any free or sorbed organic liquid in the tuff below the shafts, implying that the organic liquids released from the waste shafts have fully volatilized. The organic vapors emanating from the subsurface, liquid waste must migrate through the subsurface before reaching the atmosphere. Large amounts of the liquid waste have volatilized to create the current plume of organic vapor in the subsurface. The vapor plume has migrated over 100 meters laterally from the shafts as demonstrated by pore-gas sampling, and it is estimated to contain nearly 1000 kg of vapor-phase VOCs [LANL, 1999]. Pore-gas sampling shows that VOCs disposed of at this site include 1,1,1-trichloroethane (TCA), trichloroethylene (TCE), trichlorotri-flouroethane (FREON), and lesser amounts of chloroform, toluene, benzene, cyclohexane, methyl chloride, and other similar solvents.

The purpose of this work is to develop a calibrated numerical model for the vapor plume beneath MDA L that can be used to analyze the current and future state of the plume. In this report, we develop a diffusion model for TCA transport at the site that predicts the migration of the vapor-phase plume from the shafts through the subsurface. The model assumes that the movement of the vapor plume can be described through its most prevalent component, TCA. It also assumes that plume growth is controlled by diffusive processes rather than by air flow within the mesa top. The model is calibrated to pore-gas data collected at the site. Simulations of several different cases that use various diffusion coefficients, source-term concentrations, and boundary conditions are

examined. The best-fit simulation is determined with a goodness-of-fit scheme that compares the different model results to the field data. We found that the predicted subsurface concentrations match observed pore-gas concentrations quite well for a few of the better simulations, indicating that the diffusion model adequately describes plume behavior. The model is applied to predict plume growth over the next 50 years, to suggest monitoring frequency, and to estimate the possible system response to the bursting of a buried drum. In a future study, the model will be used to explore schemes for site corrective measures.

2.0 - SITE DESCRIPTION

2.1 STRATIGRAPHY AND TOPOGRAPHY

The strata that immediately underlie MDA L are composed of nonwelded to moderately welded rhyolitic ash-flow and ash-fall tuffs interbedded with thin pumice beds. The rhyolitic units are underlain by a thick basalt unit, and a conglomerate formation [Krier, et al., 1997]. The tuff layers were deposited during violent eruptions of volcanic ash from the Valles Caldera between 1.2 and 1.6 million years ago [Smith and Bailey, 1966; Gardner et al., 1986]. Since then, the tuff has eroded to leave a system of alternating finger-shaped mesas and canyons. MDA L is located atop one such mesa, Mesita del Buey, with the waste disposed in shallow pits (4 m deep) and shafts (approximately 20 meters deep). The surrounding canyons, Canada del Buey and Pajarito Canyon, lie 30 m below the steep-sided mesa, and the regional aquifer is located approximately 300 meters below the disposal pits. There are no known perched aquifers below the mesa. Figure 2.1_1 shows the site topography and the locations of disposal pits, disposal shafts and monitoring wells.

Figure 2.1_2 shows a simplified stratigraphic column of the rocks underlying MDA L. The upper three stratigraphic units make up the Tshirege member of the Bandelier Tuff. Unit 2 and the lower half of the Unit 1v are fractured. The Cerro Toledo interval is comprised of volcanoclastic sediments interbedded with minor pyroclastic flows, and separates the Tshirege and Otowi Members of the Bandelier Tuff. The Otowi Member is nonwelded to poorly welded and is not fractured. The units comprising the Bandelier Tuff dip gently and thin toward the eastern end of the site [Vaniman et al., 1998].

The following subdivisions and thin units are not included in Figure 2.1_2 or in the numerical model domain. The Tshirege Unit 1v is generally subdivided into units 1v-u and 1v-c. Units 1v and 1g are separated by a thin horizon known as the vapor-phase notch, which is easily seen in outcrop, but is not necessarily continuous and additionally is too thin to include in a site-scale model. The Tsankawi Pumice, a thin (20-100cm) bed at the base of Unit 1g, is lumped into Unit 1g in the model. There are surge beds at the bases of both Tshirege Unit 2 and Unit 1 which are not included in Figure 2.1_2 or in the site-wide geologic model [Vaniman et al., 1998]. The Otowi is subdivided into an ash-flow component and a pumice fall that are not separated in Figure 2.1_2 or in the site-wide geologic model. Although these units can be hydrologically significant, their effect on the diffusion equation is minimal, as only the diffusion coefficient and the moisture content of a given unit affect the diffusion solution. As we'll show later, a uniform diffusion

coefficient is chosen for the modeling, and the site moisture content does not vary by more than an order of magnitude. Therefore, excluding these units should not strongly affect the solution.

The Cerros del Rio Basalts, which comprise nearly 50% of the unsaturated zone, display wide variability [Turin, 1995], ranging from extremely dense with no effective porosity, to highly fractured, to so vesicular as to appear foamy. The Puye Formation underlies the Cerros del Rio Basalts and extends from the of base of the unsaturated zone well into the saturated zone. The Puye Formation is an amalgamation of alluvial fan, river, and lake deposits containing cobbles and boulders of both volcanic and plutionic origin in a matrix of silts, clays, and sands. Interbedded basalt flows, dacite flows, and pumice lenses are also common [Purtymun, 1995].

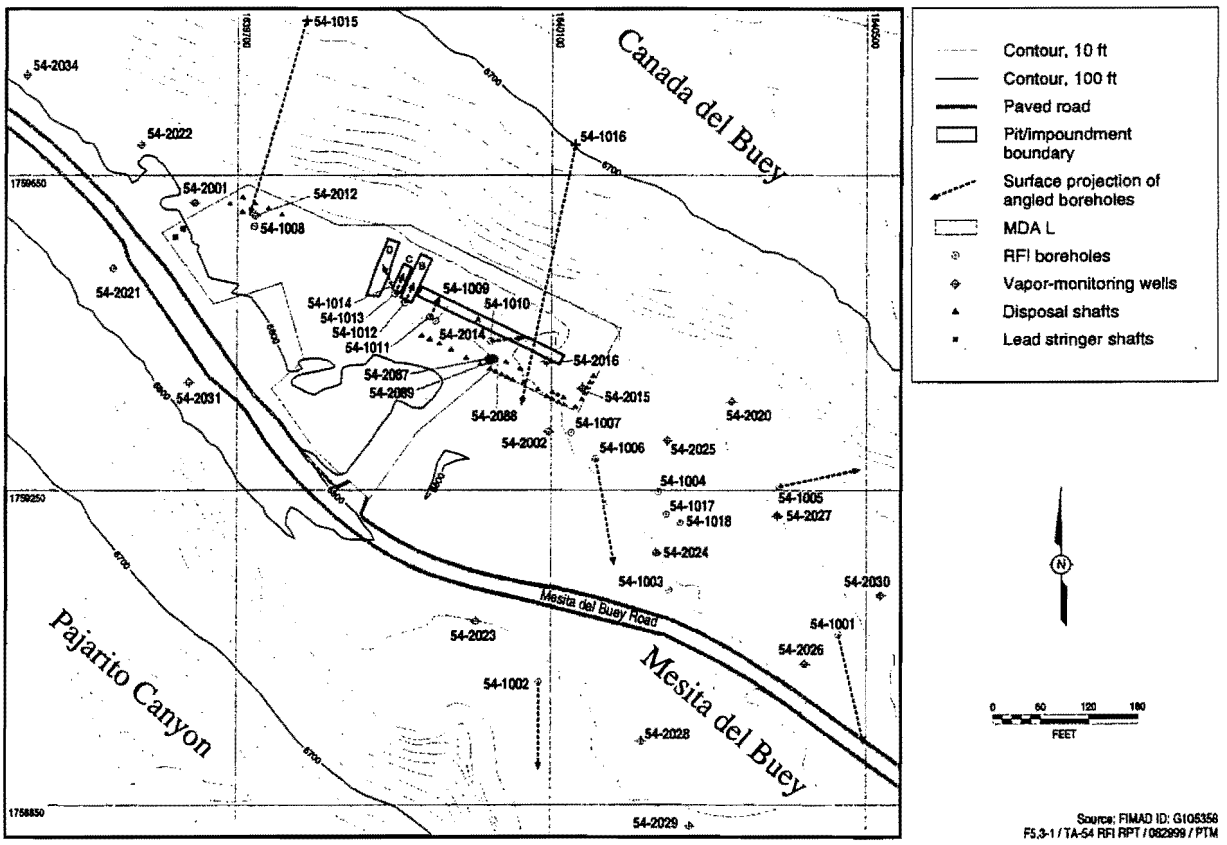

Figure 2.1_1 Geographical information for MDA L and the surrounding area.

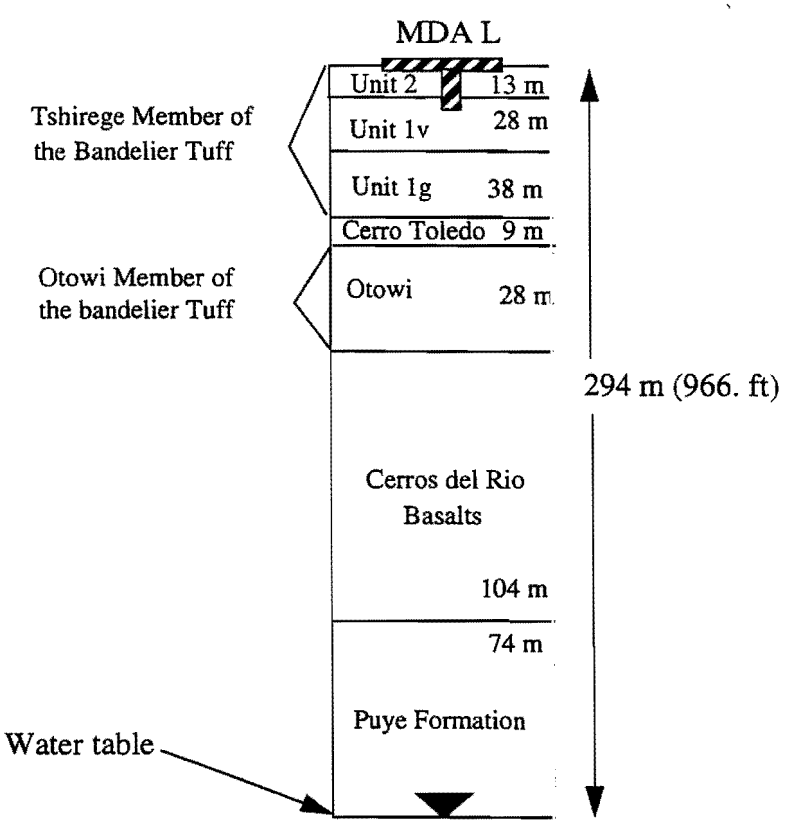

Figure 2.1_2 Simplified site stratigraphy.

2.2 CONTAMINANT SOURCE

MDA L was used as a disposal site for liquid chemical waste from the late 1950's until its closure in 1986 [LANL, 2000]. After passage of the Resource Conservation and Recovery Act (RCRA), regulations concerning the disposal and storage of hazardous waste caused the Laboratory to discontinue subsurface disposal of hazardous mixed waste. Both solid and liquid mixed and hazardous wastes are currently stored above ground in facilities at MDA L that allow the waste to be inspected and monitored before removal to permanent disposal facilities.

2.2.1 Timing of waste disposal at MDA L

One pit, three surface disposal impoundments, and 34 disposal shafts are the Potential Release Sites (PRS) at MDA L (Figure 2_2.1) [LANL, 2000]. These PRSs had varying purposes and were used for different time periods. Disposal Pit A was the only disposal unit in operation before 1975. Dates of operation for Pit A were from 1964 until 1978. Surface impoundment B was established in 1979 and decommissioned in 1985. Impoundments C and D were in use from 1985 to 1986 and 1972 to 1984 respectively.

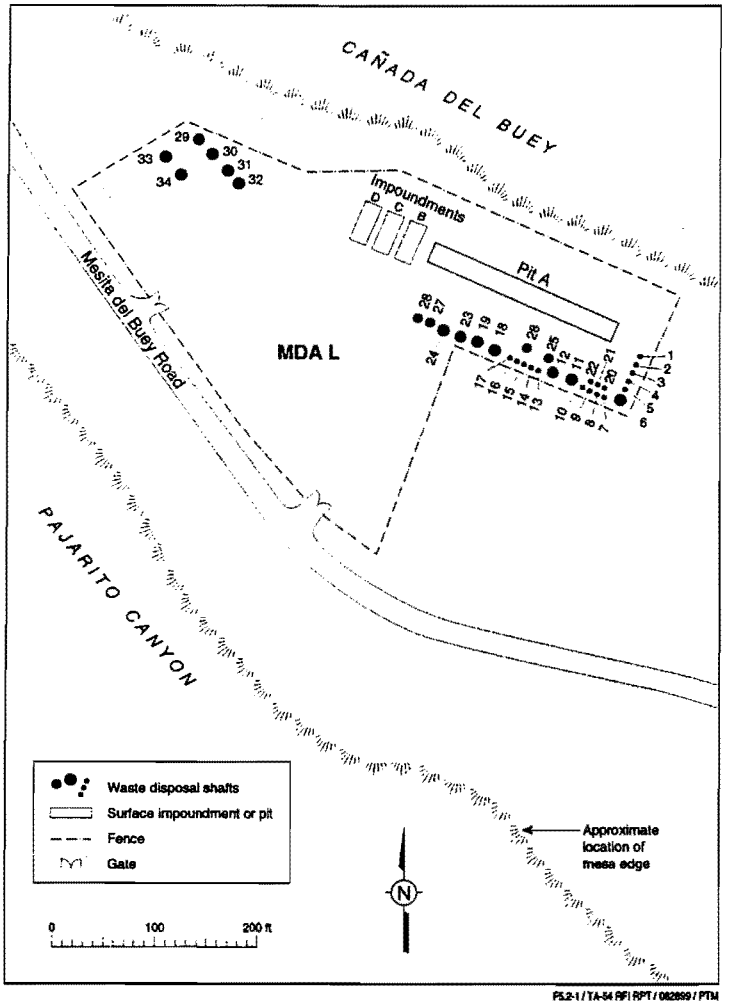

Figure 2.2_1 Location map for waste disposal shafts and pits at MDA L

Operation dates for the 34 disposal shafts ranged from 1975 to 1985. Shaft numbers 1 through 28 operated from 1975 through 1985, while shaft numbers 29 through 34 operated from 1983 through 1985. After decommissioning, most of the 2.5 acres comprising MDA L were covered with asphalt upon which were built temporary storage facilities for hazardous mixed waste. The asphalt covering affects the subsurface transport of the VOCs as discussed in Section 2.3.2.

2.2.2 Types of waste found at MDA L

There is little information on specific chemicals, timing, or quantities of waste that were disposed of at MDA L. However, the major COPCs measured at this site are found in pore-gas sampling and include a host of volatile organic compounds (VOCs) and tritium [LANL, 2000]. Pit A received non-containerized bulk quantities of treated aqueous waste that was left to pool and evaporate without added absorbent material. This waste is not reported to contain VOCs. However, if some VOCs were disposed of in Pit A, their high vapor pressures would have led to quick

evaporation into the atmosphere. Therefore our conceptual model of MDA L does not include Pit A as a source of VOC vapor in the subsurface.

Surface Impoundments B, C, and D were exclusively used as evaporative lagoons for treated salt solutions. Salt solutions such as ammonium biflouride and electroplating wastes were a source of copper, barium, chromium, and zinc contamination in the impoundments [LANL, 2000]. Records indicate that the majority of waste disposed of in the surface impoundments was inorganic, therefore these disposal units are not included as a source term in the simulations of the VOC vapor plume.

The 34 shafts received metal drums (55 gallon) containing both hazardous and mixed liquid waste. The waste drums were packed in lifts with one to six barrels per layer. In the shafts, layered waste was covered with crushed tuff to provide absorbent material as well as structural support for the drums. Additionally, unknown quantities of small containers and free product were dropped directly into the shafts. The locations of the pits and shafts can be seen on Figure 2.2_1. Shaft numbers 1 through 28 are located near Pit A, while shaft numbers 29 through 34 are located 60 m northwest of Pit A. The spatial distribution of the waste led to two main source regions for organic vapors, causing the development of the double-lobed plume seen in the site data (Figure 2.2_2). Records indicate that the majority of material placed in the shafts was organic waste. The records do not differentiate between pure liquid and organic contaminated solids (rags, paper, etc.). However, because MDA L is a designated liquid waste disposal area, contaminated solids were most likely disposed of at MDAs C and G. For these reasons, a source term for the organic liquids can only be roughly defined. The major long-term source for organic contamination in the disposal shafts is expected to be from potential future releases as a result of drum deterioration.

Sampling conducted to determine the existing VOC plume in rock core and pore gas from various boreholes on or near the site found a vapor-phase plume that consists primarily of TCA, TCE, carbon tetrachloride, and chloroform [LANL, 2000]. That study found no evidence for free liquid or sorbed organics in 170 core samples from 18 boreholes [LANL, 1999]. Peak concentrations of TCA vapor found below the bottom of the shafts suggests that some limited liquid transport of VOC may have occurred prior to the core studies [LANL, 2000].

The major vapor-phase contaminant measured in the second quarter of FY99 was TCA, which composed approximately 75% by volume of the spatially averaged plume. The second most prevalent contaminant found was TCE, comprising 12.5% by volume of the plume, while Freon 113 composed 11.2% by volume of the averaged plume. These values are averaged over

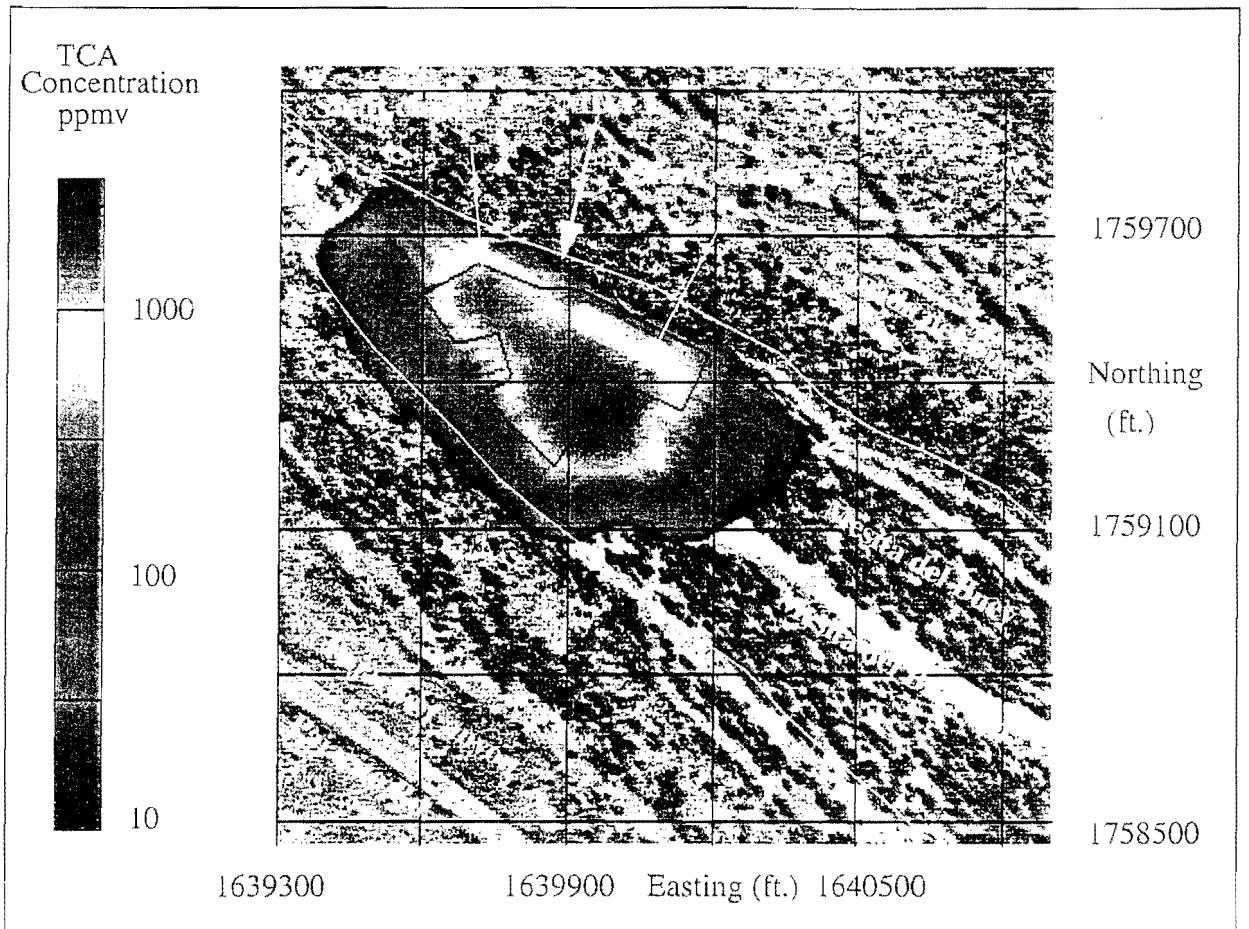

Figure 2.2_2 Second Quarter FY99, MDA L, TCA concentration data (log-scale) contoured on a plane 18 m (60 feet) below the mesa top.

140 sampling locations measured using the B and K field-screening method, which detects only TCA, TCE, and Freon. Although these numbers are spatial averages, individual sampling ports show wide variation in the ratios of the most prevalent VOCs, and the more complete analytic laboratory analyses show some ports (for example, well 54-2032 at 47.5 m (156 ft) below the collar) have significant percentages of compounds such as napthalene (12%) and dichloroethene 1,1 (14%) [Smith et al., 1999b].

2.2.3 Pore-gas monitoring data

Quarterly pore-gas monitoring has been conducted at the site since 1985 in accordance with a compliance ordered issued by the state of New Mexico [LANL, 2000]. Continued monitoring of soil gas has shown that the organic vapor-plume source region is coincident with the disposal shafts, and that the plume does not appear to have grown at a detectable rate over the past three years [Smith et al., 1998, 1999a, 1999b]. In fact, the current maximum TCA pore-gas concentration is similar to the value of 3400 ppmv reported by Trent [1992] in data from June. 1988.

The individual shafts that have contributed the largest portion of the plume are not well defined, and the simulations we present are designed to capture the general behavior of the main

source regions. Figure 2.2_2 shows the second quarter FY99 monitoring data of measured TCA concentration at a depth of 18.3 m (60 ft.) below the mesa top contoured in map view. The data have been clipped at 10 ppmv to represent the lower limit of data reliability, which is 5 to 10 ppmv.

2.3 CONCEPTUAL MODEL and MODEL ASSUMPTIONS

The conceptual model on which the numerical simulations are based contains several key features [Rogers, 2000]. We assume that VOC migration at the site can be described by the diffusive transport of TCA vapors. Although some advective processes, such as barometric pumping, may enhance plume migration, Auer et al. [1996] showed that this can be modeled as enhanced diffusion. The plumes, however, do not grow as ideal spherical plumes because several external factors influence their shape. These factors include nonideal boundary conditions such as the topography of the site, the asphalt cover, and the venting of the plume through the deep basalt unit. Disposal history and source location also contribute to nonspherical plumes.

2.3.1 Unsaturated-Zone Transport Processes

As suggested by the preliminary conceptual model [Rogers, 2000], we assume that diffusion is the fundamental process controlling migration rates of TCA in this unsaturated environment. Diffusion moves chemicals from areas of high concentration to areas of low concentration [Fetter, 1999]. Diffusion is caused by random motion of molecules and is a function of both temperature and the chemical's molecular weight. Thus, chemicals with a low molecular weight diffuse more rapidly at a given temperature. The effect of diffusion is to homogenize an initially heterogeneous distribution of chemical concentrations. The speed at which a chemical diffuses is described by the diffusion coefficient, D. D is much larger in air than in water, thus a drop of dye in water spreads more slowly than, for example, perfume spreads in air. Also, diffusion is slower in a porous medium than in free space because of the tortuous nature of small pores. Typically, a porous medium diffusion coefficient D* is 1/2 to 1/100 the value in free space [Freeze and Cherry, 1979].

One goal of this study is to test the assumption that a simple first-order diffusion model fits the pore-gas data. Estimates for a reasonable diffusion coefficient in the tuff are based on core-scale measurements, however we also consider the possibility that diffusion is effectively increased by barometric pressure changes in the more fractured units (Tshirege Unit 2 and Cerros del Rio Basalts). Other processes (time-dependent barometric pumping, wind effects, and liquid

transport of TCA) may need to be included to fit second-order variation in the data, and these additional processes may be examined with respect to the long-term development of the vapor-phase contaminant plume (>50 years) [Rogers, 2000] in future studies.

2.3.2 The effect of system geometry on plume growth

Because MDA L is located on the edge of a narrow finger mesa, the interaction of the subsurface vapor-phase contamination with atmospheric air must be considered [Rogers, 2000]. The topographic relief of the mesa provides an atmospheric boundary condition of near zero concentration [Mishier and Anderson, 1994] where the plume intersects the mesa top and sides. Because diffusion occurs from areas of high concentration to low concentration, the atmospheric boundary provides a huge sink, or low concentration volume, that can accept the VOCs that diffuse from the subsurface. This boundary maintains a steep concentration gradient between the subsurface plume and the mesa sides, which limits plume growth along the axis of the mesa.

Additionally, Neeper [1997] reports that the air in the basalt appears to be much more connected to the atmosphere than the air in the Bandelier tuff. We hypothesize that a low concentration boundary, similar to the atmospheric boundary, exists in the basalt unit. We test the hypothesis by fixing the concentration in the basalt at an atmospheric (zero) concentration of TCA in some simulations during model calibration.

The presence of the asphalt at MDA L potentially affects the ability of TCA vapor to migrate upward into the atmosphere. For this reason we test the sensitivity of the system with sealed asphalt (choosing $D^* = 1\text{x}10^{-14}$ m^2/s to effectively stop diffusion through the asphalt), leaky asphalt (choosing $D^* = 4\text{x}10^{-7}$ m^2/s to allow limited communication of the source with the atmosphere above the asphalt), and no asphalt.

2.3.3 Release and mobility of TCA vapor

The migration of TCA vapor from the shafts is conceptualized as a time-release phenomenon. This is based on the idea that liquid will leak slowly from the buried drums and quickly volatilize in the subsurface. Once released from the shafts, we assume the mobility of TCA through the unsaturated zone is controlled by diffusion along concentration gradients. The steepest concentration gradients will form along pathways to the atmosphere [Fetter, 1999].

Migration of TCA in the liquid phase is not included in the model, because there are no observations at the site of saturated conditions in the subsurface. In fact, moisture monitoring shows that the current subsurface moisture profiles are near background conditions, despite the

previous disposal of liquid waste at the site [LANL, 2000]. The pore-gas concentrations also clearly indicate that no migration of free product (pure TCA) occurs. If pure-phase TCA were in the pores, its vapor pressure would yield pore-gas concentrations from one to two orders of magnitude larger than the highest concentrations observed in the monitoring data.

2.4 HYDROGEOLOGIC DATA

This study deals strictly with vapor-phase diffusion in the subsurface of MDA L. Therefore, the subsurface flow of water and air is decoupled from the diffusive transport. The major parameters affecting diffusive vapor transport are porosity, saturation, and the porous medium diffusion coefficient (D*). The porosities and saturations are fairly well characterized for the six Bandelier Tuff units. The porosities and saturations for the tuff units [Rogers and Gallaher, 1995] and the Guaje Pumice were measured on core samples of tuff. Estimated values for the porosity and saturation of the Puye Formation are used. No hydrologic property data were available for the basalts at the time this study was performed. Therefore, the porosity of a vesicular basalt located beneath Idaho National Engineering Laboratory is used as an analog [Bishop, 1991]. The saturation of the basalt is based on previous modeling results [Birdsell et al., 1997]. Fortunately, the model of the contaminant plume is relatively insensitive to the properties of the Puye Formation and Cerros del Rio Basalts. Table 1 summarizes the hydrologic parameters used for all of the units in the unsaturated-zone flow and transport model.

Table 1: Physical Parameters used in the numeric model, bold indicates the base simulation

Unit	Effective porosity	In-situ saturation	Effective diffusion coefficient (10^6xD* in m^2/s)
Tsh 2	0.48	0.05	1, 2, **4**, 8, 20
Tsh 1 v	0.51	0.04	1, 2, **4**, 8
Tsh 1 g	0.48	0.2	1, 2, 3, **4**, 8
Cerro Toledo	0.473	0.3	1, 2, **4**, 8
Otowi Member	0.435	0.25	1, 2, **4**, 8
Cerros del Rio basalt (matrix)	0.23	0.25	1, 2, **4**, 8, 20
Puye Formation	0.25	0.25	1, 2, **4**, 8
Shafts	0.5	0.05	1, 2, **4**, 8

Table 1: Physical Parameters used in the numeric model, bold indicates the base simulation

Unit	Effective porosity	In-situ saturation	Effective diffusion coefficient (10^6xD* in m^2/s)
Asphalt	0.5	0.05	**$1x10^{-8}$**, 0.4, 4
Surface (not including asphalt)	0.48	0.05	1, 2, **4**, 8, 20

2.5 TRANSPORT PROPERTIES

The modeling uses an estimate for the subsurface, vapor diffusion coefficient (D*) of the predominant vapor-phase contaminant, TCA. The initial estimate of the diffusion coefficient for TCA vapor (D*= $4x10^{-6}$ m^2/s) is based on core-scale measurements of TCA diffusion in Bandelier Tuff from TA-54 [Fuentes et al., 1991]. The model is run with a range of diffusion coefficients centered on the core-scale results to determine which diffusion coefficient best fits the site data. Because the diffusion coefficient of TCA in asphalt is unknown, we examine the sensitivity of the system to two values of the diffusion coefficient through the asphalt. In the first case, we assume a diffusion coefficient of $1x10^{-14}$ m^2/s in the asphalt, which essentially stops the contaminant from mixing with the atmosphere in asphalt-covered regions. In the second case, we assume the asphalt is leaky, with D* = $4x10^{-7}$ m^2/s, allowing some mixing of the source with the atmosphere above the asphalt.

3.0 - NUMERICAL MODEL OF TCA TRANSPORT AT MDA L

The MDA L site model is a three-dimensional representation of the hydrogeologic system, including the surface topography. The numeric modeling is limited to diffusive transport in the subsurface and reduces the complexity of the problem by neglecting water flow (infiltration), air flow (barometric pumping and wind effects), Henry's law phenomenon (solubility of the vapor contamination in the aqueous phase), and dispersivity (increased mixing due to airflow). These simplifications are suggested by the preliminary conceptual model [Rogers, 2000].

The simulations are run with FEHM, a three-dimensional finite-volume heat and mass transfer code suitable for simulating systems with complex geometries [Zyvoloski et al., 1997]. The governing equations in FEHM arise from the principles of conservation of water mass, air mass, contaminant mass, and energy. Darcy's law is assumed to be valid for the momentum of the air and water phases. The advection-dispersion equation, which governs solute transport in FEHM [Fetter, 1999; Zyvoloski et al., 1997], becomes the diffusion equation under no-flow conditions. Water flow is restricted by using van Genuchten [1980] parameters that result in no appreciable water flux. Air convection is damped by fixing a horizontally stratified temperature gradient in the model domain. This results in air velocities that are negligible relative to the diffusivity of the contaminant and allows us to better understand the process of diffusion within the mesa.

3.1 MODEL DOMAIN AND COMPUTATIONAL GRID

The model domain covers a rectangular map area with the southwest corner at State Plane (SP) coordinate (1639275,1758825) and the northeast corner at SP coordinate (1640625,1759775). The model uses SI units, and the SP data (feet) were converted to meters for the simulation. The grid is 411 m (1350 ft.) wide in the x direction (east-west) and 290 m (950 ft.) in the y direction (north-south), as shown in Figure 3.1_1. The land surface in the model domain is based on Digital Elevation Model (DEM) data, which allow accurate representation of the major features of the mesa/canyon system. The grid uses a subset from the DEM data to approximate the surface with 15-m spacing. The model surface shown in Figure 3.1_1 compares favorably to the site topography seen in Figure 2.1_1. Node spacing is 15.24 m (50 ft.) in both the x and y directions, and is variable in the z direction from a minimum spacing of 1 m (3.3 ft.) to a maximum of 15.24 m (50 ft.). The node spacing was chosen to assure a final grid that will compute in a reasonable time frame (on the order of 1 hour for a 10 year simulation) while maintaining the basic site topography. Model

geometries of the subsurface hydrogeologic units are based on interpolated data from existing boreholes and outcrop, and are of a lower resolution than surface geometry.

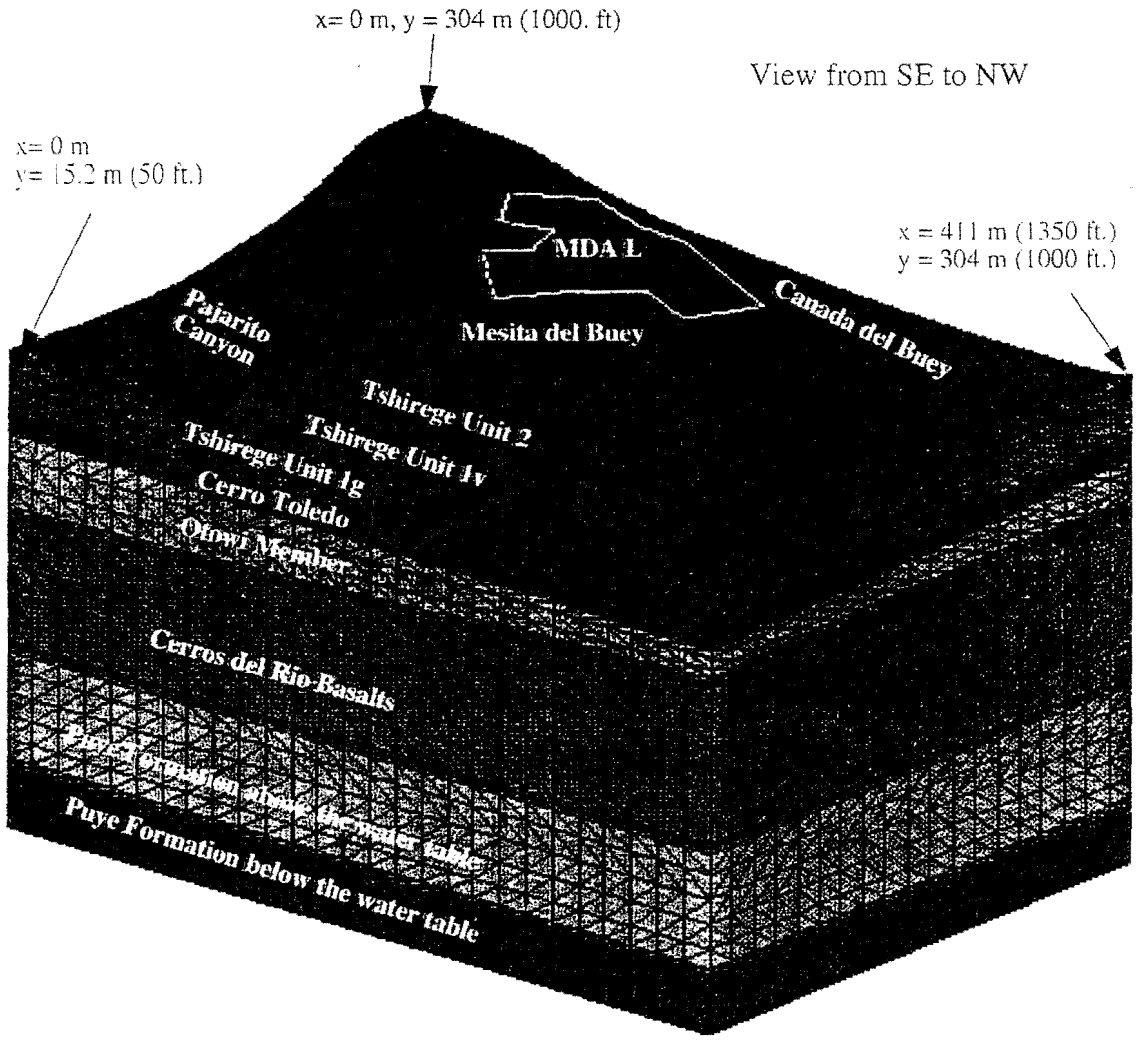

Figure 3.1_1 Model topography and computational grid

The model domain extends vertically from the land surface to below the water table and delineates a rectangular volume of over 43 million cubic meters. The stratigraphic configuration used for the model (Figure 3.1_2) is derived from the LANL site-wide geologic model [Vaniman et al., 1998]. Surfaces and interfaces are loaded into the LaGrit grid generation software [Trease et al., 1996; George, 1997], and a computational grid is formulated that maintains positive definite coupling coefficients at all volume interfaces. Furthermore, the stratigraphic interfaces are given higher-resolution node spacing to allow for sharp gradients in material properties. The final grid contains 25,456 nodes and 147,438 tetrahedral volume elements.

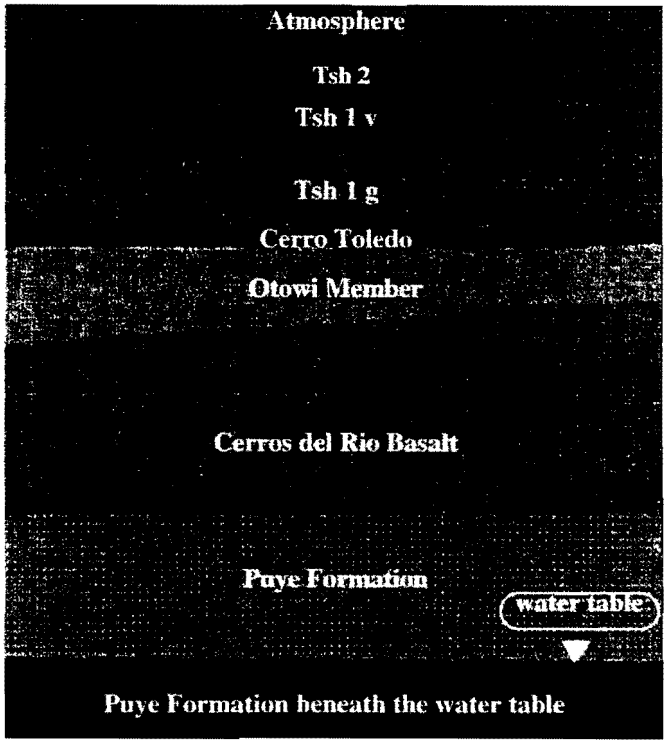

Figure 3.1_2 Model stratigraphy for cross-section B-B' (see Figure 4.3.1_2).

3.2 BOUNDARY AND INITIAL CONDITIONS

The bottom boundary of the domain is flat and lies below the water table. The presence of the water table within the model domain allows us to estimate travel times to this important horizon. No flow of water or vapor is permitted across the bottom boundary, and its temperature is held constant at 25°C, based on well bore measurements [Griggs, 1955]. The atmosphere at the top of the model is held at a pressure of 0.078 MPa, and the temperature is fixed to the yearly average of 10°C [LANL weather website]. The atmosphere is represented by fixing the concentration at zero in the nodes above the land surface. The vertical side boundaries of the domain are no flow with respect to both mass and heat.

Before running the contaminant transport simulations, a static air pressure field is established by running the model until pressures and temperatures reach equilibrium. This ensures that the transport simulations are not affected by transient behavior associated with establishing a static air pressure field. The steady-state initial condition has no TCA present and is meant to represent the mesa before release of contaminants.

3.3 SHAFTS AND ASPHALT

The model node spacing is too coarse to explicitly include each shaft found at MDA L. Therefore, we group the shafts into two clusters, with cluster #1 containing shafts 1 through 28 and cluster #2 containing shafts 29 through 34. Each cluster is specified using three nodes which include a volume of the model domain (3520 m^3) extending from two meters below the surface to a depth of approximately 20 meters (60 ft.). The model shafts coincide spatially with the two actual shaft clusters shown in Figure 2.2_1. TCA is introduced to the model shafts based on a simplification of the available data. The shaft nodes are assigned fixed concentrations of TCA based on the highest measured concentrations from vapor ports near the shafts. Because maximum measured concentrations vary through time, we simulate both high (11,000 ppmv) and low (3000 ppmv) fixed concentration sources in the shafts.

The asphalt cover is modeled as having been laid down as one layer at the beginning of 1985. The timing of the asphalt cover is not well documented, and our approach is meant to capture the gross system behavior. The spatial location of the asphalt is based on the site map and personal communication from Dennis Newell that 98% of MDA L is paved. In addition to the extensive asphalt covering within the boundaries of the site, substantial portions of the mesa around MDA L have been paved for parking lots, trailer foundations, and roads [Site visit, Jan. 2000]. The modeling presented below includes only the asphalt within the boundaries of MDA L. The aerial extent of the asphalt covering is identical to the site boundaries and can be seen in Figure 4.1.2_1. The asphalt restricts surface flux to the atmosphere. Future modeling may include more detailed representation of the surrounding asphalt and structures as data become available.

The time-varying site model is run in three stages to capture the main events that occurred during the emplacement of waste at MDA L. We begin all the contaminant transport simulations in 1975 by fixing TCA concentrations in shaft cluster #1. The simulation is halted at 1983 to add shaft cluster #2, then restarted and run until 1985, at which time the asphalt is added to the mesa top. The simulations is again restarted and run to 2000 and beyond. The above simplification of the sequence of events at MDA L is justified based on the limited site data and the need to minimize the complexity of the simulations.

3.4 SUMMARY OF LOGIC FLOW FOR THE BASE SIMULATION

The first simulation we present uses our initial best estimate for the in-situ effective diffusion coefficient and other important hydrogeologic parameters. We refer to this initial model as the base simulation (Table 1). We create a set of results for the base simulation to which we compare results for simulations with variations in boundary conditions (asphalt vs. no asphalt), variations in the TCA effective diffusion coefficient (D*), and variations in source concentration.

The base simulation is initiated in 1975 when shaft cluster #1 (representing shafts 1-28) is fixed to a concentration of 3000 ppmv and held at this concentration throughout the simulation. This source is allowed to diffuse until 1983 when the model is halted to add shaft cluster #2 (representing shafts 29-34). The second shaft cluster is then also fixed at 3000 ppmv for the duration of the simulation. The model is restarted and run until 1985. Finally, the asphalt cover is added, and the model is run until the year 2000. The base simulation results in approximately 865 kg of TCA in the modeled plume at the year 2000. The method for modeling the TCA source is reasonable given the sparse data on disposal operations at the site. The TCA mass generated with this method also compares favorably to the integrated mass of the measured TCA vapor plume, which yields a value in the range of 1000 kg based on data from 1999 [LANL, 1999].

4.0 - RESULTS

4.1 BASE SIMULATION RESULTS

4.1.1 TCA concentrations through the model domain

Figure 4.1.1_1 shows the predicted TCA concentration in the year 2000 for the base simulation with a TCA diffusion coefficient of 4 x 10^{-6} m^2/s. The figure is a two-dimensional

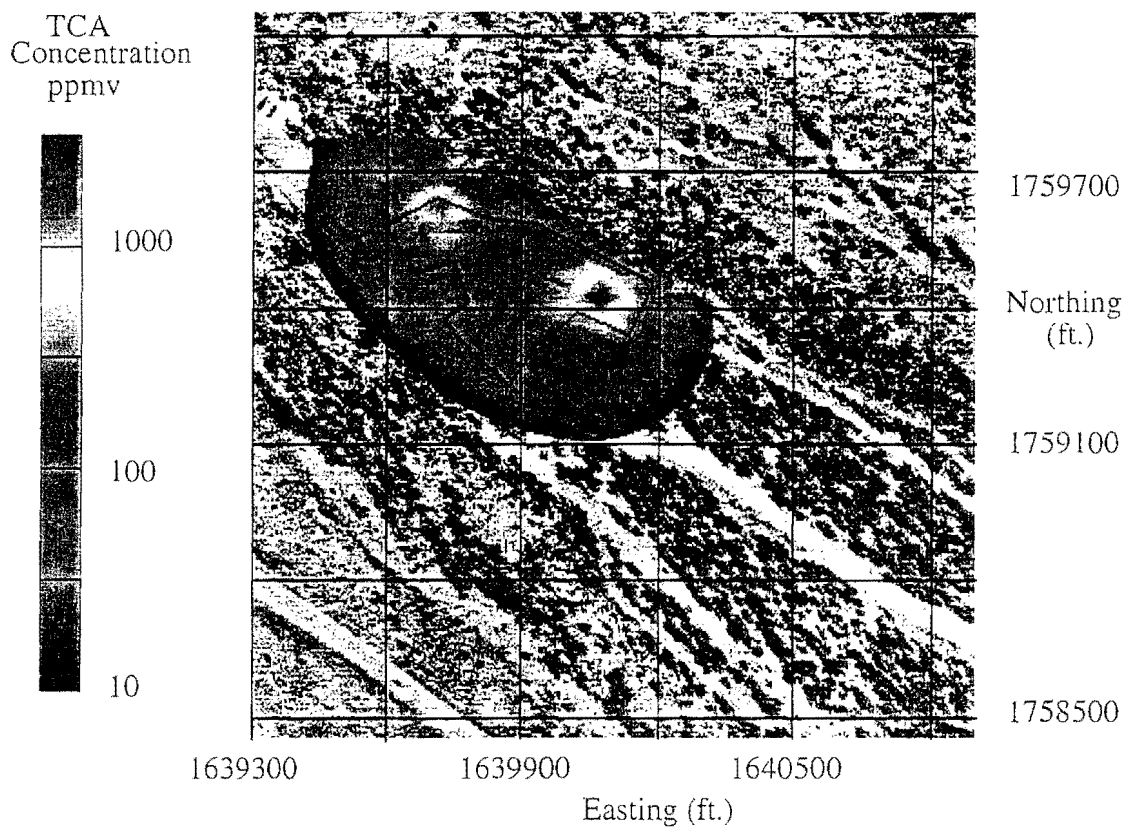

Figure 4.1.1_1 TCA concentration (log scale) for the base simulation contoured on a plane 18 m (60 ft.) below the mesa top.

horizontal slice of the model domain at a depth of approximately 18 m (60 ft.) below the top of the mesa. The concentrations are shown in powers of ten (log scale) to allow regions of both high and low concentrations to be visualized. The maximum concentration (red) of 3000 ppmv TCA shows the locations of the shaft clusters. The edges of the mesa are clearly visible as areas where concentrations drop quickly to near zero (darkest blue). The plume at this depth is spreading along the axis of the mesa, while TCA is being removed from the system along the mesa edges. As discussed in the conceptual model, the atmospheric boundary at the mesa edge is expected to give

rise to the high concentration gradient along Canada del Buey that is evident in the figure. This figure can be compared directly with the monitoring data shown in Figure 2.2_2. The most obvious similarities are the shape of the plume and the location of the highest concentrations near the two shaft clusters. The 10 ppmv contour outline in both figures covers approximately the same areal extent.

Several differences are evident as well between the data and the simulation. The first is that the two source areas are not as pronounced in the data as in the model results. The data are not gathered at regularly spaced intervals and therefore require interpolation for the visualization. The data presented here are interpolated with a nearest neighbor scheme. Monitoring data are gathered near the two shaft clusters but not near the center of MDA L (Figure 2.1_1). Because of this, the nearest neighbor interpolation scheme yields higher concentrations between the two concentrated source regions than calculated by the diffusion model. For this reason, visual interpretation in itself cannot be used to assess the quality of the calibration. In a later section, we present a goodness-of-fit analysis that is used to determine the best-fit simulation.

Another difference between the data and the simulation is seen on the north boundary of the model domain where the model's no-flow boundary becomes apparent. At this boundary, TCA is unable to leave the system, leading to higher concentrations than seen in the data. The effect of the no-flow boundary is explored later in simulations by fixing this boundary at zero concentration rather than as no flow.

Figure 4.1.1_2 is a comparison of TCA concentration for the data and the base simulation contoured on a horizontal plane at a depth of 49 m (160 ft.) below the mesa top. The extent of the 10 ppmv contour of the simulation matches the data very well over most of the domain. Again the source regions differ and the effect of the no-flow northern boundary is evident in the simulation results.

4.1.2 Surface flux

Figure 4.1.2_1 shows the predicted surface flux of TCA at the interface between the ground surface and the atmosphere. The calculated fluxes use the modeled concentration at the surface diffusing over one meter to the zero concentration atmosphere. The location of the simulated asphalt is seen as the dark blue patch overlying the outline of MDA L. Flux through the asphalt is very low because the asphalt is modeled with a very low diffusion coefficient that forces the TCA to diffuse by an alternate path to the surface. The effects of the asphalt on surface flux are clearly seen by the high fluxes around the edge of the site. Because TCA flux is controlled by

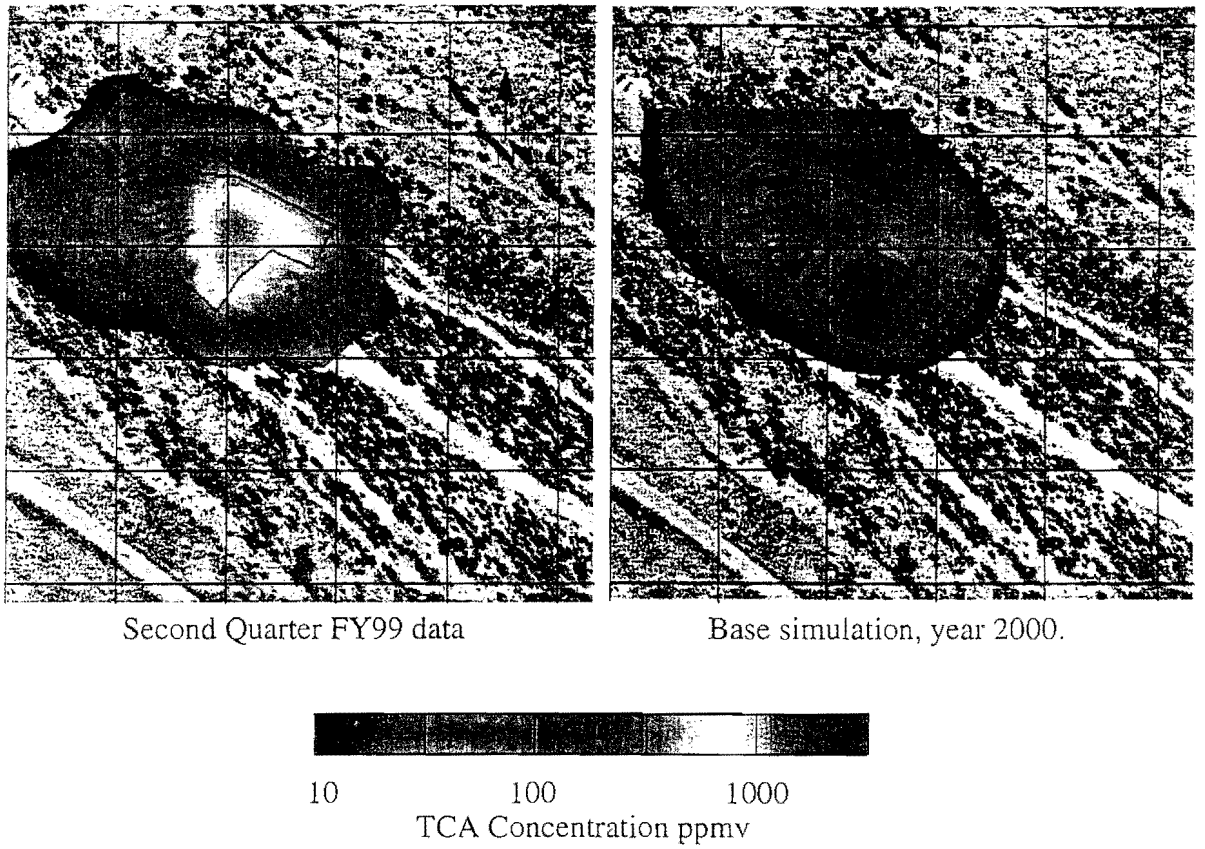

Figure 4.1.1_2 TCA Concentration for the data versus the base simulation on a plane 49 m (160 ft.) below the mesa top.

concentration gradients, the model predicts that the highest loss of TCA to the atmosphere occurs along the edges of the asphalt, the shortest path from the high concentration source to the atmosphere. The wall of Canada del Buey, immediately to the north of the site, also has high concentration gradients and is important in removing TCA from the subsurface. The high surface fluxes seen along the northern boundary of the model domain are artifacts of the no-flow boundary condition and should not be interpreted as physically significant.

In the base model, 1780 kg of TCA are lost to the atmosphere during the simulation. This loss represents nearly 70% of the 2645 kg of TCA mass input during the simulation. Our surface flux results compared qualitatively to surface flux chamber measurements performed in 1993 that show high fluxes around the edge of the site boundary and on the slopes of Canada del Buey to the north [Trujillo, 1998]. Quantitatively, however, the maximum computed surface flux from the model (0.1 kg/(m^2 yr)) is nearly 300 times higher than the maximum values reported for the sampling (668 ng/(m^2 min) = 0.00035 kg/(m^2 year)). The calculated surface flux uses the modeled

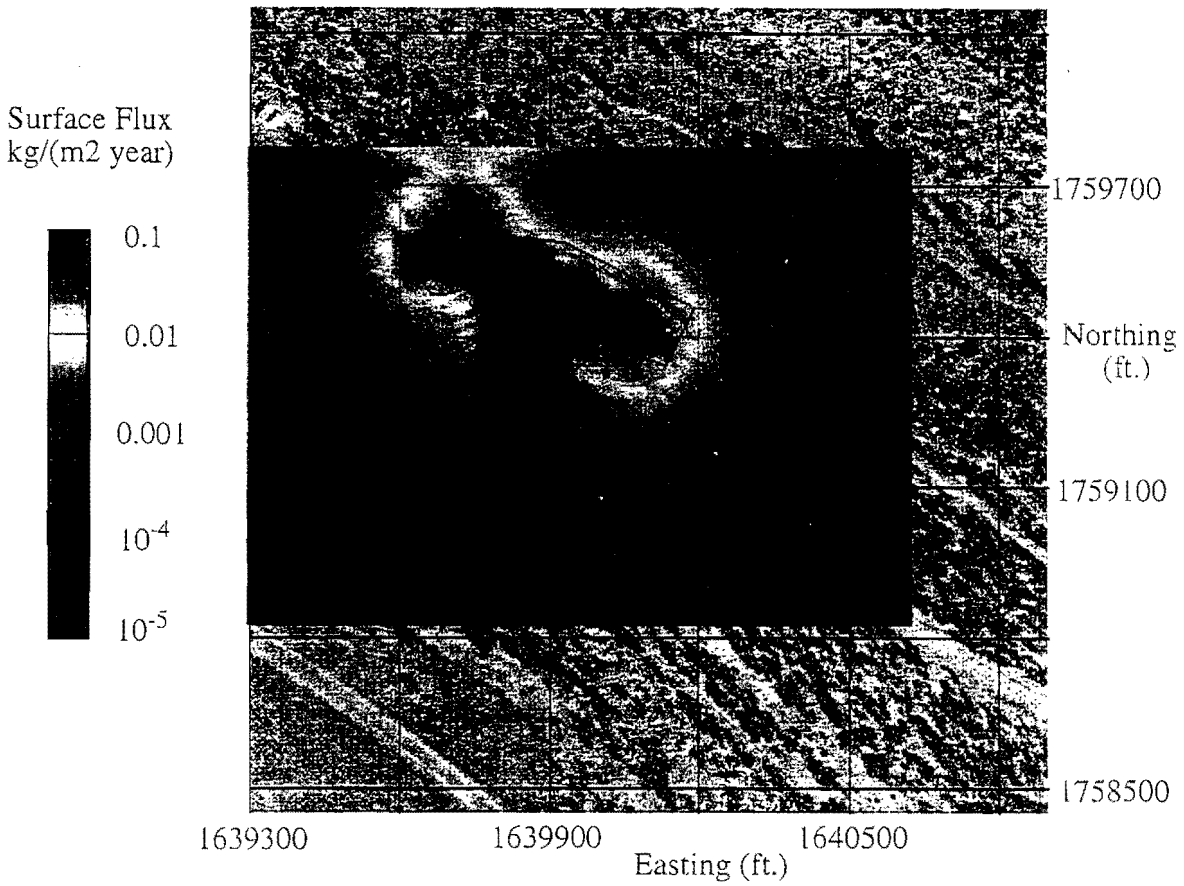

Figure 4.1.2_1 Flux of TCA to the atmosphere for the base simulation.

near-surface concentrations of TCA in combination with $D^* = 4x10^{-6}$ m^2/s and an assumed one meter transition to the atmosphere to calculate surface flux as:

Surface Flux = D* x (Model C at a surface node/ 1 meter)

We also performed a back-of-the-envelope calculation based on the observed near-surface concentrations of TCA (approx. 1000 ppmv) in well 54-2089 at a depth of 4 meters and assumed $D^* = 4x10^{-6}$ m^2/s. One thousand ppmv is equivalent to 0.001 (moles TCA)/(mole air). One m^3 of air is about 34.5 moles. Thus there are 0.034 moles TCA/(m^3 air). TCA contains 133 g/mole yielding 4.6 grams of TCA per cubic meter of air. Calculating the flux to the surface using these numbers gives: Surface flux = D* x (dC/dz) = $4x10^{-6}$ m^2/s x (4.6 g/m^3)/(4 m) = 4.6 x 10-6 g/(m^2s) = 0.144 kg/(m^2 yr), which agrees well with the maximum model surface flux of 0.1 kg/(m^2 yr). We believe that this discrepancy between the simulated and the measured surface flux may be affected by systematic measurement error. One source of possible error in the measurements is that 5.4 centimeters of rain fell during the sampling period, which could decrease the ability of organic

vapor to diffuse to the surface. Furthermore, nearly half of the 15 samples sent out for EPA review showed TCA concentrations in excess of the linear response range of the calibration [Trujillo, 1998]. These problems were noted in the TA-54 RFI report, and for this reason the surface flux data are used only qualitatively to describe the extent of the plumes at MDA L [LANL, 2000].

4.1.3 Goodness of fit of the base simulation

To analyze the goodness of fit between the model results and the monitoring data (Second quarter, FY99), we calculate the mean (μ) and standard deviation (R) of the relative error of the model as a percentage of the data (PE = model/data) [Boas, 1983]. Percent error is used instead of the more traditional absolute residual (model - data) to capture the three order of magnitude variation in the data. Using this scheme, values for PE are greater than 1 when the model is higher than the data, and less than 1 when to the model is less than the data. To generate meaningful statistics, the values less than 1 are renormalized as the negative of the inverse of the value which can be expressed as a logical statement: If PE < 1. then PE = -1*(1/PE). Thus, when the model is higher than the data, PE ranges from 1 upward, and when the model is lower than the data, PE ranges from -1 downward. The values are then shifted to PE = PE - abs(PE)/PE. This results in an ideal mean that lies at zero and allows a standard deviation about the mean to be calculated consistently for the various simulations. To avoid infinite percentages when the data are very close or equal to zero, we choose a lower cut-off of 10 ppmv and consider the model to be in agreement with the data when both values are below the lower cut-off. The reliability of the data falls as values approach 5 to 10 ppmv and this fact provides further justification for the chosen cut-off.

We also employ a conditional statement that is designed to flag potentially spurious data points or sections of the model domain that are extremely different than the data. This condition states that if the ratio, model/data, is greater than 3 or lower than 0.33, the model/data pair is flagged and removed from the calculation of the mean and standard deviation. The number of points removed is counted and reported along with the statistical properties to determine goodness of fit for the base simulation as well as other simulations presented later. This gives us a consistent approach to differentiate simulations and find the model parameters that yield the best overall fit to the greatest number of monitoring points. Future fitting should include all relevant data sets, perhaps with quality control at the level of the data collectors to remove questionable data based on intimate knowledge of the sampling apparatus and site-specific problems. Such quality control would help tremendously in yielding meaningful results.

Using the logic outlined above, the base simulation gives a mean of -0.068 and a standard deviation of 0.72, with 29 of the 142 data points removed from the calculation [Table 2]. The mean model result is therefore only 6.4% below the data, with one standard deviation including values from (1.72 x data) on the high side to (0.58 x data) on the low side. This is a good fit considering the simple nature of the parameters used in the simulation.

4.2 MODEL BEHAVIOR WITH VARIATION FROM THE BASE SIMULATION

We next present a series of simulations that explore variations in the base model. Results are shown in Table 2 for several scenarios.

Table 2: Goodness of Fit for various simulations

Changes from the Base simulation	mean	Standard Deviation	Points removed
None (Base simulation)	-0.068	0.72	29
no asphalt	-0.24	0.69	31
leaky asphalt	-0.13	0.69	28
$D^*=1x10^{-6}$ m^2/s	-0.23	0.52	44
$D^*=8x10^{-6}$ m^2/s	0.0015	0.69	44
Basalt C = 0.	-0.072%	0.71	24
N. and W. C = 0.	0.089	0.68	18
N., W., and B.; C = 0.	-0.093%	0.67	15

B. = basalt; N. = North boundary; W. = West boundary; CT = Cerro Toledo, S. = surface

First, we simulated the site with no asphalt. The number of points lying outside the cut-off for this case is slightly larger than the base case (N = 31 vs. 29), however the mean of -0.24 is much lower and implies that the simulated concentrations are lower than the measured concentrations at more points. The standard deviation is nearly the same implying that both simulations spread equally about their respective means. The results for the leaky asphalt ($D^*=4x10^{-7}$ m^2/s) are shifted similarly toward the model underestimating the data. Thus, the asphalt at MDA L appears to be best fit as a non-diffusive barrier forcing VOC's to migrate downward and laterally to reach pathways that lead to the atmosphere.

We next explore the effect of varying the porous-medium, vapor diffusion coefficient. When D* is doubled from the base case to $8x10^{-6}$ m^2/s, 44 points fall outside the cut-off, and the mean is positive showing that the simulated concentrations overestimate the data. When D* is quartered from the base case to $1x10^{-6}$ m^2/s, 44 points again fall outside the cut-off, and the mean lies well below zero, showing that the simulated concentrations are lower than measured concentrations. Because both of these simulations have more points lying outside of the cut-off, the base simulation is seen to be a better fit to the data.

We explore the effects of the no-flow boundary and of the potential of the basalt to rapidly exchange pore gas with the atmosphere by fixing these sections of the model domain to zero concentration. When the basalt is fixed to zero concentration, there are 24 points lying outside of the cut-off, whereas when the north and west boundaries are fixed to zero, there are only 18 points removed. Combining these two simulations results in only 15 points removed and a slightly improved standard deviation.

Figure 4.2_1 shows the data versus model regressions for all simulations except the 'no asphalt' and 'leaky asphalt'. This series of plots helps to show differences between the individual simulations in a graphical manner. In an ideal model, the regression would plot exactly on the 1:1 line, which is shown in red on Figure 4.2_1.

Figure 4.2_2 shows another way of representing the data versus model regression. The regression is now in the form log10(model) versus log10(data). Log(10) is used to reduce the dominance of high values that occurs when a simple model versus data regression is performed. Most importantly, there have been 10 points deemed to be spurious data removed from each of the simulations and the data. These 10 points were found to lie outside the statistical cut-off used for most of the simulations, and the individual points removed were checked by hand to ensure that they meet criterion for being spurious data (i.e. values that change radically from one quarter to the next, or values that are unrealistically low or high for their position in the plume). This figure shows the same trend as seen in Figures 4.2_1 as well as in Table 2. The different simulations are clearly separated graphically and show that the best-fit simulation has the north and west boundaries and the basalt fixed to zero concentration (NWB; standard deviation (R) = 0.94, intercept (I) = 0.095; slope (S) = 0.88), in complete agreement with Table 2. The base simulation yields R = 0.844, I = 0.44, and S = 0.72 showing that the base simulation is overestimating concentration data at the low end while underestimating data at the high end. The D* = 1e-6

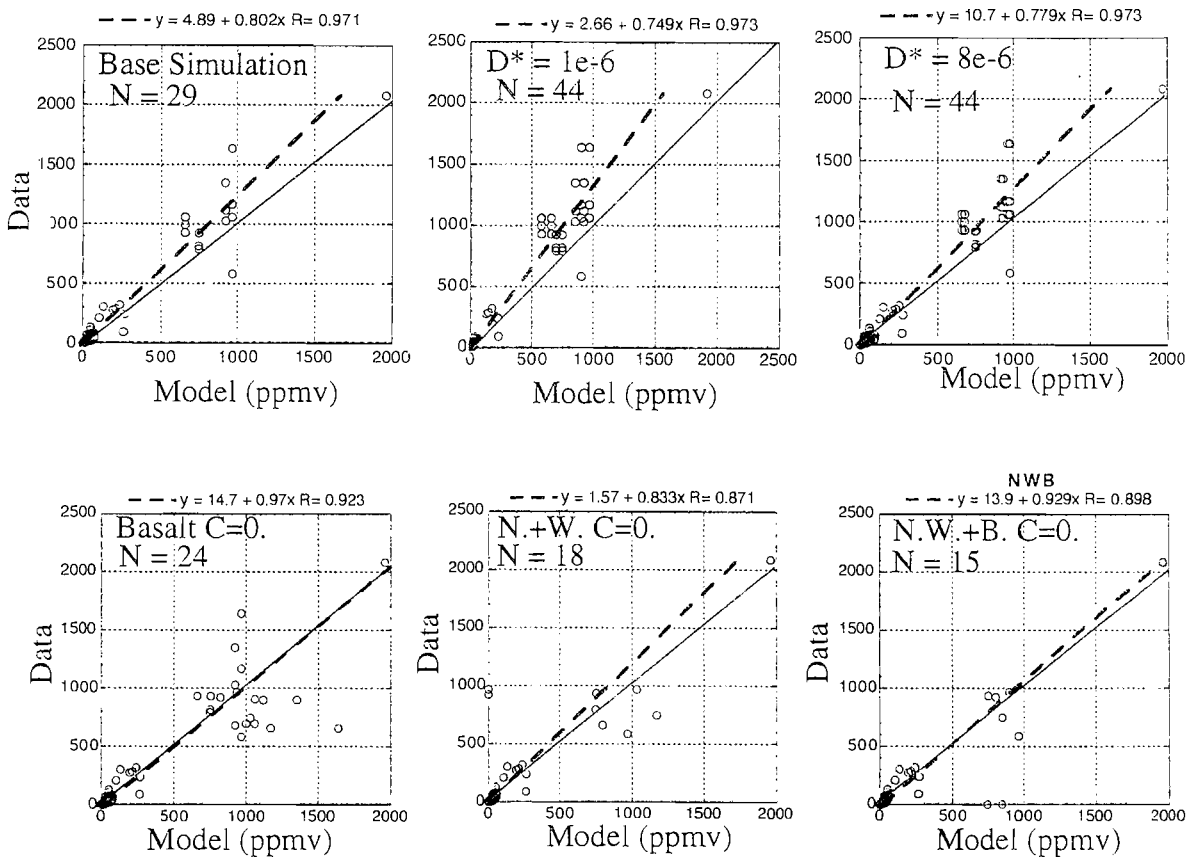

Figure 4.2_1 Regression plot of simulations presented, based on GOF statistics. Points flagged by the upper and lower cut-off in the statistical logic (N) have been removed from these plots.

simulation (labeled as 1D) intercept (I = -0.19) lies well to the left of the 1:1 line and has R = 0.88 and S = 0.82, while the D* = 8e-6 simulation yields I = 0.79, R = 0.80, and S = 0.59.

Not shown on Figure 4.2_2 are the no-asphalt, leaky asphalt, fixed basalt, and fixed north and west boundary examples. The leaky and no asphalt cases have intercepts which plot well to the right of the 1:1 line and both have R = 0.84. The fixed basalt example has R = 0.88 and an intercept of 0.3. The fixed north and west boundary case (NW) has R = 0.84.

4.3 RESULTS FROM THE BEST-FIT SIMULATION

4.3.1 Basic results

The best-fit simulation maintains the north and west boundaries and the basalt at a concentration of zero for all times. The justification for fixing the basalt to zero comes from observations that the air pressure in the basalt is in phase with and of the same magnitude as the atmospheric pressure. The north and west boundaries are set to zero concentration to minimize

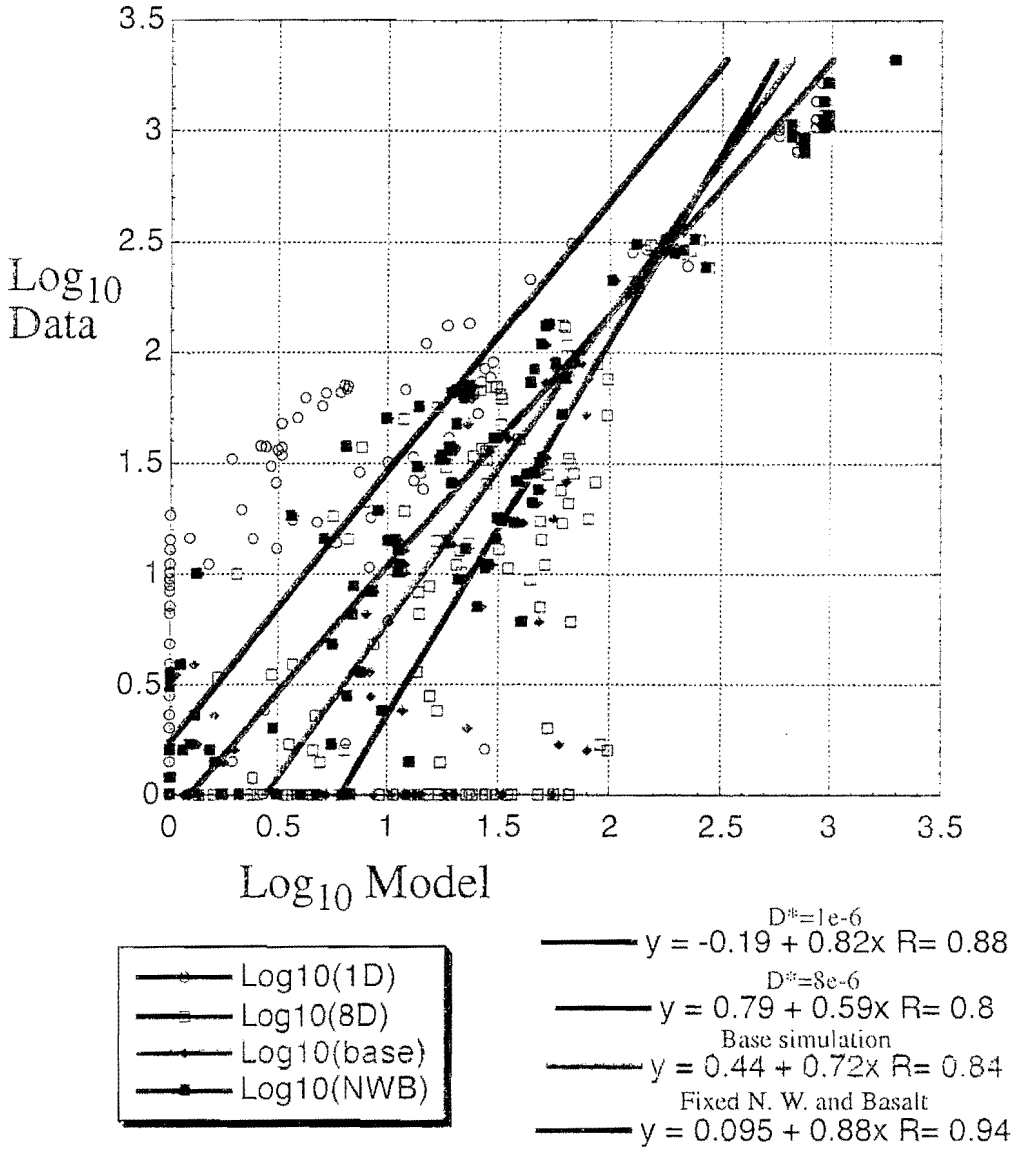

Figure 4.2_2 Regression plot of simulations presented, based on removing potentially spurious data.

boundary effects caused by the size of the model domain. Figure 4.3.1_1 shows the effect of fixing the boundaries and basalt to C=0. on concentrations in the deep domain. The base simulation results in a plume that reaches much further into the basalts. The concentrations seen in the best-fit scenario are much closer to the data and support the idea that the basalt is readily exchanging air with the atmosphere.

For the best-fit simulation, we next show a more detailed look at the distribution of the plume, both along the axis of the mesa and perpendicular to the axis of the mesa. Figure 4.3.1_2 shows the relationship of the plume to the geologic units on a cross-section B-B′ running through MDA L perpendicular to the mesa top. Figure 4.3.1_3 shows the relationship of the plume to the

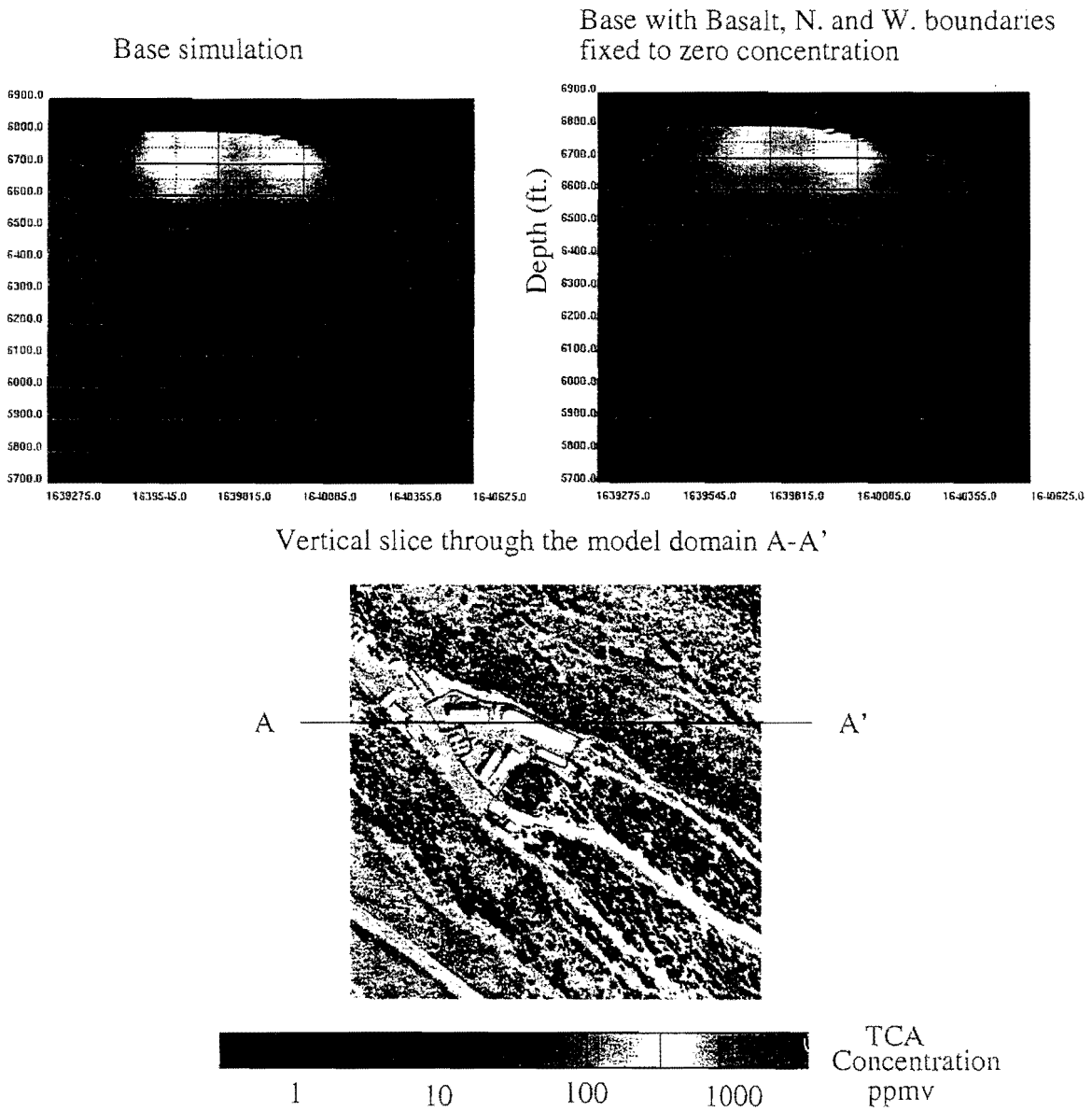

Figure 4.3.1_1 The effect of fixing the basalt, and the north and west boundaries to zero concentration on the concentrations deep in the model domain.

geologic units on a cross-section C-C′ running through MDA L along the axis of the mesa top. Boundary effects are seen in both cross-sections, at B' and at C. Boundary effects do not appear to be effecting the plume to the southeast, as shown by the smoothly varying plume in the directions of B and C'.

Another useful way to compare the base simulation with the best-fit simulation is to examine the amount of TCA in the system, the amount of TCA removed from the system, and the total amount of TCA added to the system as functions of time. This will provide quantitative estimates of absolute plume growth that are difficult to see in cross-section or horizontal slices.

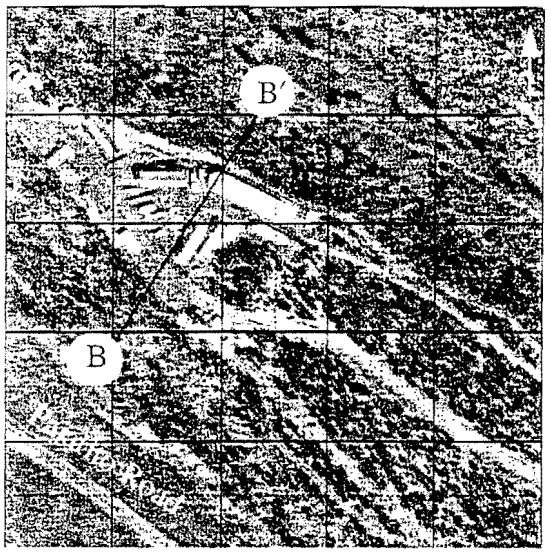

Location of cross-section B-B′

Modeled TCA concentration with depth on cross section B-B′

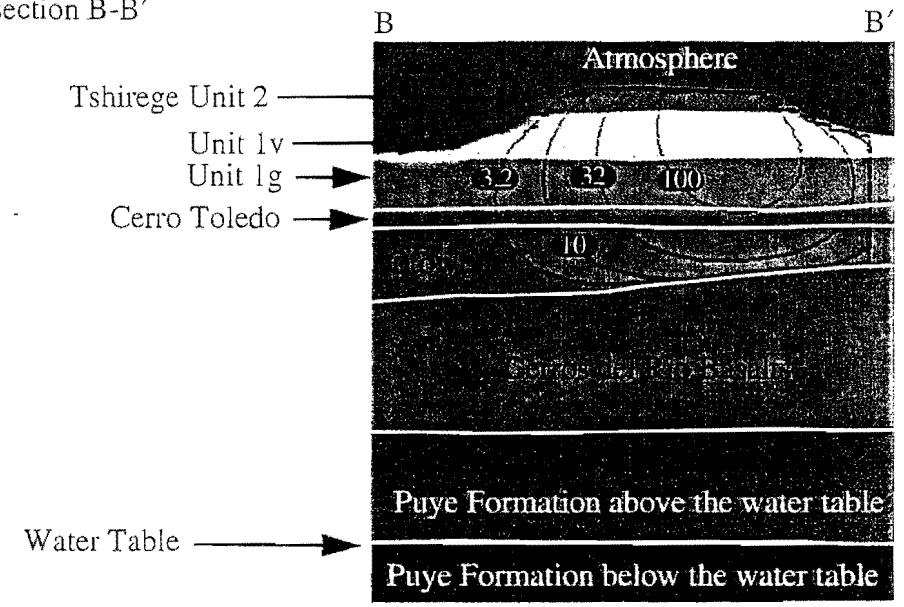

Figure 4.3.1_2 Vertical slice through the best-fit simulation (fixed N. and W. boundaries, and basalt C=0.) at cross-section B-B′. Contours are marked as TCA concentration in ppmv.

Figure 4.3.1_4 shows the total number of gallons of TCA that are in the subsurface of the model as a function of time for the base simulation and the best-fit simulation. Clearly, the best-fit simulation reaches a steady-state plume mass equal to about three 55 gallon drums full of liquid TCA. The base simulation continues to add mass to the subsurface beyond the year 2050 and leads to a plume mass equal to about five 55 gallon drums of liquid TCA. The differences in the two simulations are due to the zero concentration north and west boundary conditions, and especially the fixed zero concentration in the basalts. These two cases represent end-members, with the best-fit simulation probably underestimating the true growth of the plume, while the base simulation definitely overestimates plume growth because of the no-flow boundary effects. We next compare

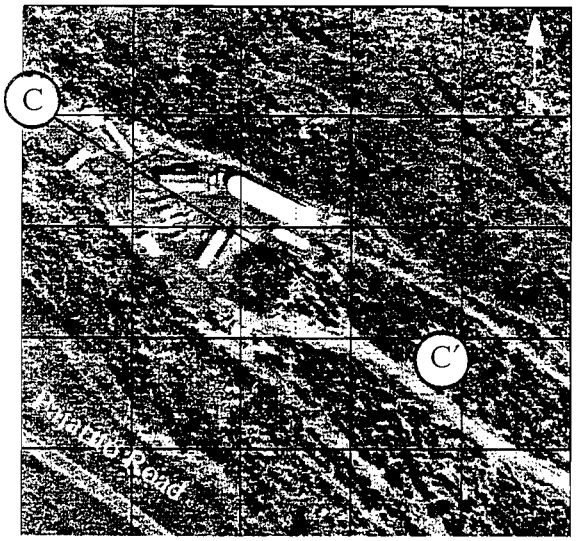

Location of cross-section C-C′

Modeled TCA concentration with depth on cross section C-C′

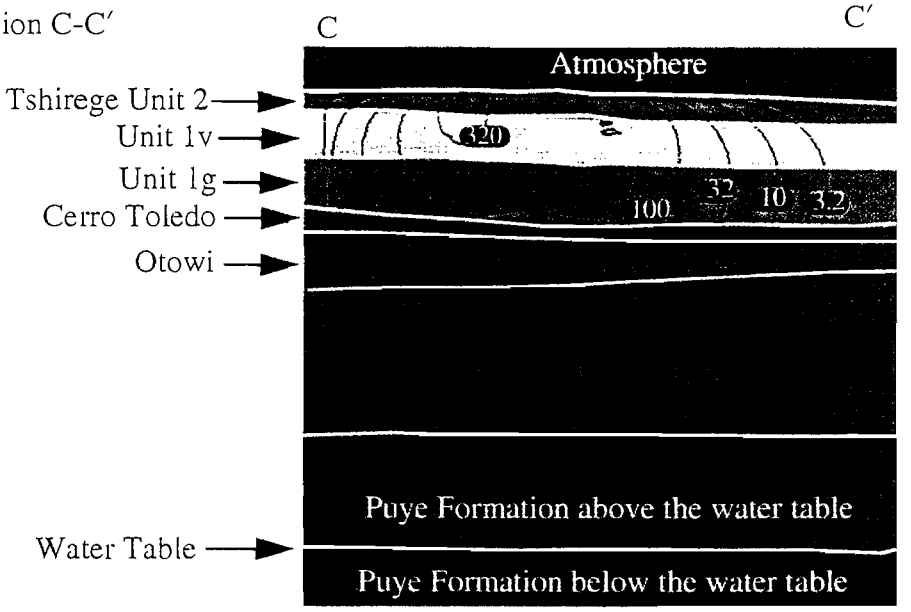

Figure 4.3.1_3 Vertical slice through the best-fit simulation (fixed N. and W. boundaries, and basalt C=0.) at cross-section C-C′. Contours are marked in TCA concentration in ppmv.

the total amount of TCA introduced from the source to the subsurface, as well as the amount of TCA that has escaped the system. Figure 4.3.1_5 shows that the amount of TCA added to the base simulation is nearly the same amount added to the best-fit simulation. The best-fit simulation, however, loses more TCA to the atmosphere (and the zero concentration basalts) and thus is able to reach a steady-state plume, as shown in Figure 4.3.1_4.

A conservative estimate for the total available source can be calculated by assuming that the shafts were filled with drums containing pure liquid TCA. There are 23 shafts having diameters of 3 and 4 feet, in which one barrel per layer was emplaced, seven shafts having diameters of 6 feet

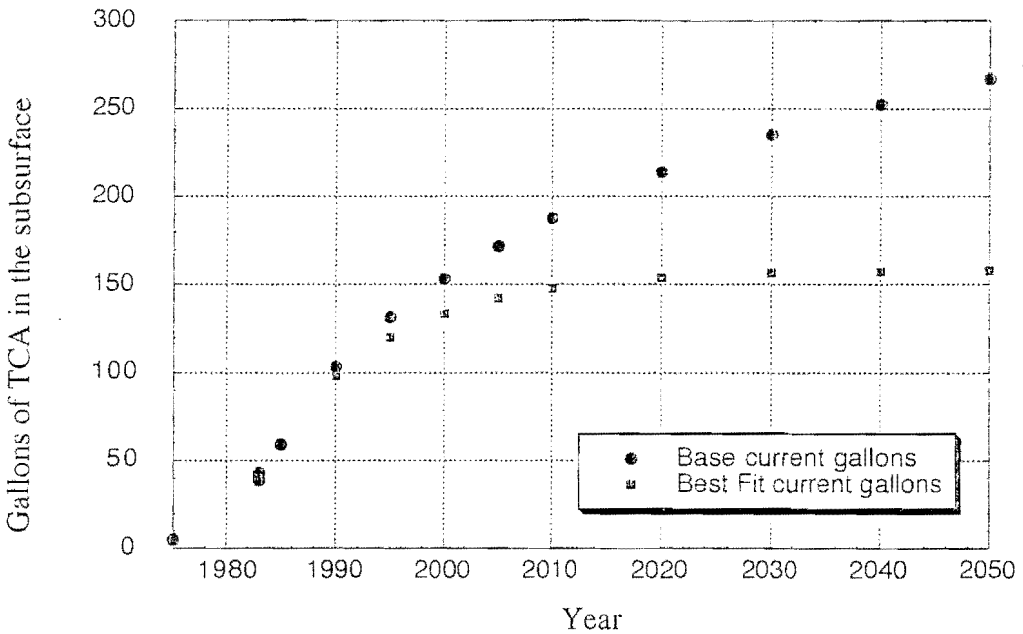

Figure 4.3.1_4 Amount of TCA in the subsurface as a function of time. Vapor-phase mass has been converted to equivalent mass in liquid gallons for comparison to waste emplacement.

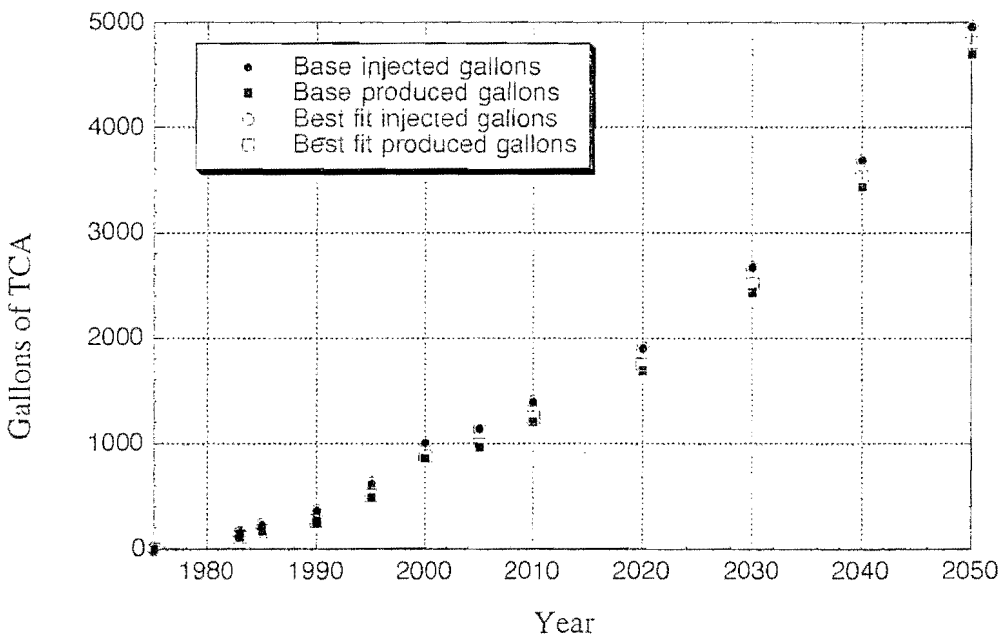

Figure 4.3.1_5 Amount of TCA injected and produced as a function of time. Vapor-phase mass has been converted to equivalent mass in liquid gallons for comparison to waste emplacement.

in which a maximum of five barrels per layer were emplaced, and four shafts having diameters of 8 feet in which six barrels per layer were emplaced. Assuming that each layer takes 4 feet and that there are 3 feet at the top used for capping the waste suggests a maximum of 14 layers of barrels per shaft. The maximum TCA source is then found by summing the total number of barrels as:

14x(7x5 + 23x1 + 4x6) = 1148 barrels (63,140 gallons) of TCA. As shown in Figure 4.3.1_5, the total amount injected into the subsurface during the simulations is less than 1/10 of the maximum possible source. A more realistic estimate of the available TCA source is probably on the order of 1/10 or less of the maximum computed value, suggesting that the contaminant source may only last until the year 2060 (or less). Once the contaminant source is completely volatilized, the plume will begin to dissipate significantly on a time scale of decades, as suggested by the relaxation time of catastrophic drum failure presented in a later section.

4.3.2 Current plume growth

Predicted pore-gas concentrations as a function of time are examined at several locations to determine the current rate of plume growth for the best-fit simulation. Figure 4.3.2_1 shows simulated concentration values at a depth of 49 m (160 ft.) for five locations to the southeast of shaft cluster #1. These locations are chosen to show the variation in concentration for regions with

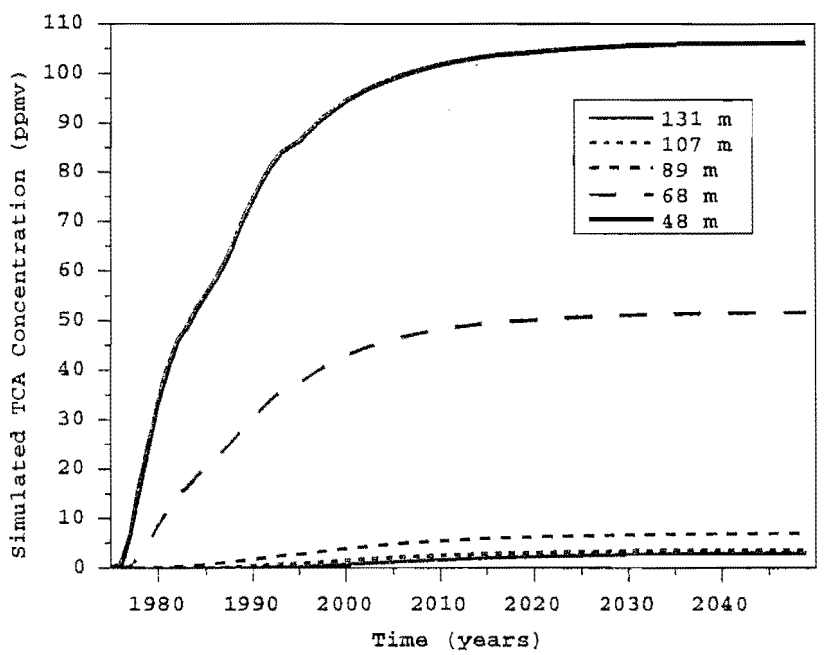

Figure 4.3.2_1 Best-fit simulation, change in concentration with time at five locations. Distance in legend shows distance to the southeast of shaft cluster #1, depth is 49 m (160 ft.) bgs.

high, medium and low values. The figure shows that the simulated concentrations change quite slowly in the year 2000. In fact, the plume is at near steady conditions, in agreement with Figure 4.3.1_4. Yearly monitoring would adequately capture the current plume growth.

4.3.3 Future plume growth: Year 2000 to 2050

The best-fit simulation was next run from the present (year 2000) to the year 2050 to demonstrate expected plume growth during the next 50 years. Figure 4.3.3_1 shows the simulation results at year 2000 (black line), year 2020 (red line), and 2050 (white line), sliced on a horizontal plane 48.8 m (160 ft.) below the mesa top. Of particular significance is the fact that the 50 ppmv

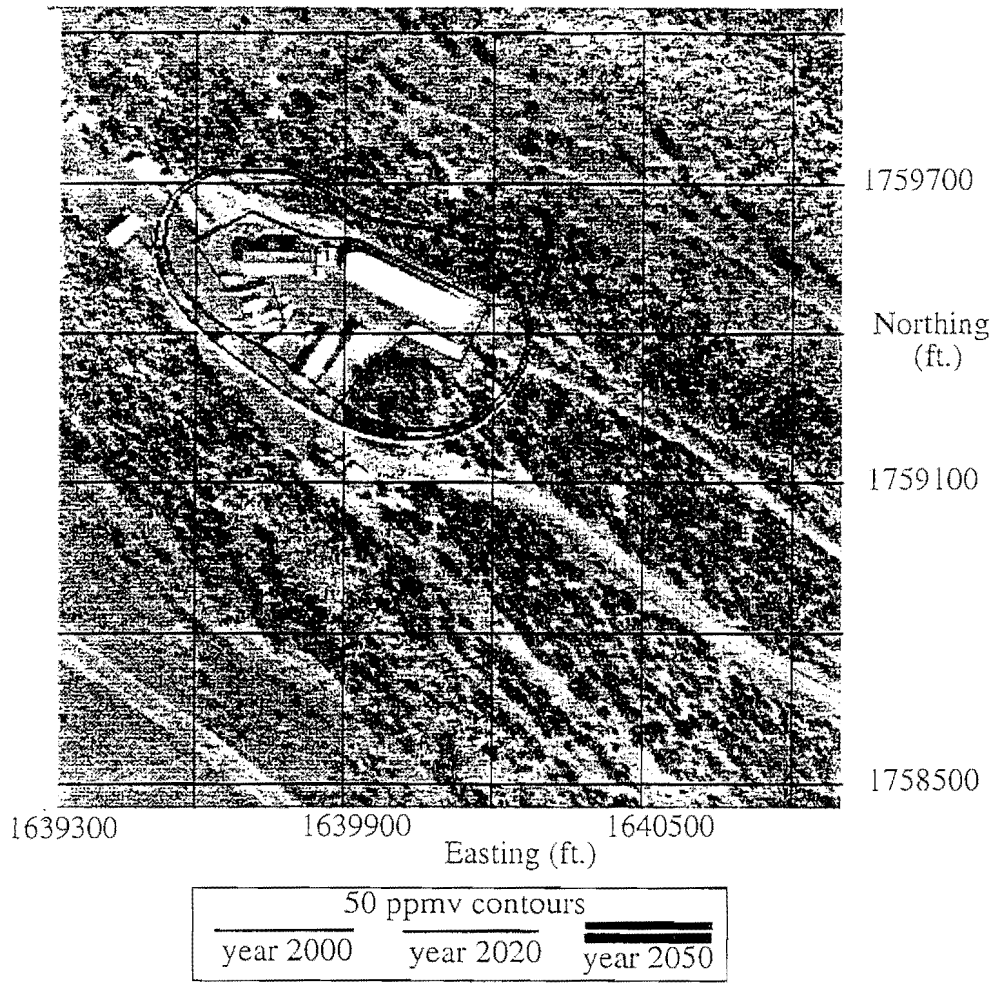

Figure 4.3.3_1 Best-fit simulation, future plume growth. 50 ppmv contours shown for the years 2000, 2020, and 2050.

contour does not move outward from the source at an appreciable rate. This is because the plume is reaching a steady-state equilibrium with the atmospheric boundary condition, where the amount of TCA released from the source over a given time is equal to the amount lost to the atmosphere. Our estimate of plume growth is conservative with respect to the size of the future plume, because the source is maintained at current levels. A less conservative estimate might include a source that decreases in strength with time. Increases in source strength are possible if individual drums of

concentrated solvent burst suddenly (Section 4.3.4), however drum corrosion data suggest slow leaking to be a more plausible scenario [Lyon et al., 1996].

4.3.4 Simulating catastrophic drum failure with the best-fit simulation

We next present the results of a simulation designed to explore catastrophic drum failure. We assume, for a worst case scenario, that approximately 55 gallons of pure TCA liquid are introduced to the system suddenly by the failure of a drum at the bottom of a shaft. The liquid flows downward, smearing homogeneously to a depth of 30 m below the shaft bottom, or 50 m below the top of the mesa. We next assume that the TCA volatilizes rapidly to create a subsurface cloud having a concentration of 20,000 ppmv. This drum failure simulation begins in the year 2000, and uses the best-fit scenario at the year 2000 as the initial condition. Figure 4.3.4_1 shows side-by-side comparisons of the best-fit simulation and the drum failure simulation in the years 2001, 2010, and 2020.

Initially, the size of the plume increases under shaft cluster #1 for the drum failure case. The 302 kg of TCA (60 gallons) that were added to the system lead to a locally elevated region of TCA concentration that extents for tens of meters laterally from the location of the failure. The extra 60 gallons injected in this simulation increases the mass of TCA in the simulation by approximately 40%, as seen in Figure 4.3.1_4. Therefore, the simulation truly represents a catastrophic event. The rate of removal of the spill from the subsurface is shown in Figure 4.3.4_2. After one year, 22% of the initial pulse from the drum failure has been vented to the atmosphere. After two years, 31% has been removed, and after five years 50% has been removed. During this time period, monitoring should be able to detect such a catastrophic occurrence, especially during the first two years following drum failure.

By the year 2010 however, monitoring will probably not be able to detect the effect from the drum failure because 70% of the original catastrophic spill is gone from the system, and the remaining 30% is beginning to spread from the source region. As seen in Figure 4.3.4_1, the plume is slightly larger directly below the source region, where the 100 ppmv contour is pulled into the Cerro Toledo. By 2020, 88% of the spill has left the system, and the plume is nearly identical to the scenario with no drum failure (Figure 4.3.4_1).

As shown in Figure 4.3.4_2, the time rate of removal of TCA from the system can be fit nicely with an exponential curve. This final result is particularly satisfying because analytical solutions to the diffusive transport equations generally follow solutions of an exponential form.

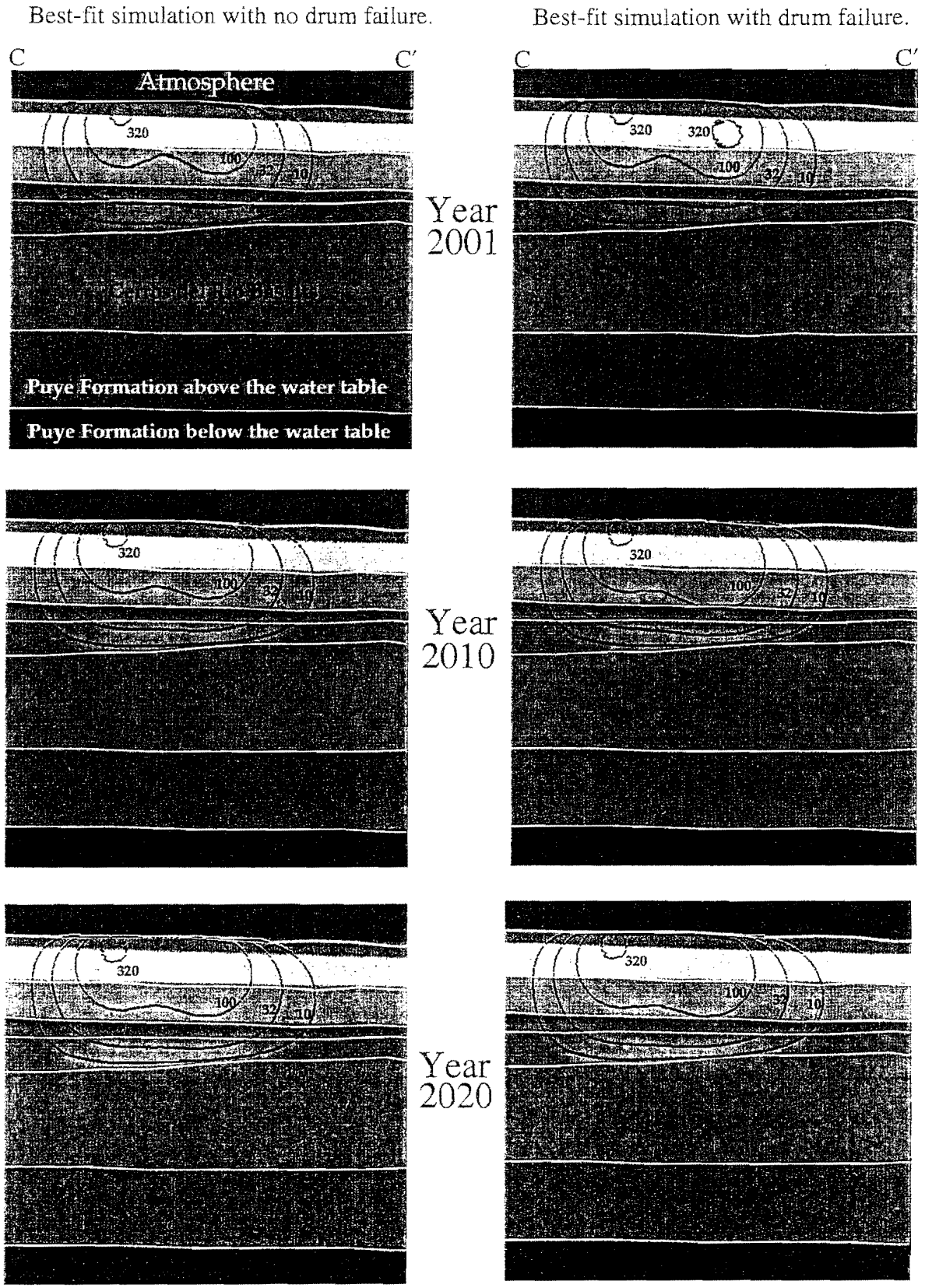

Contours lines are TCA concentration labeled in ppmv.

Figure 4.3.4_1 Comparison of no drum failure simulation with drum failure simulation. 302 kg of TCA are added as a pulse in the year 2000. Cross-section C-C′ is shown in Figure 4.3.1_3.

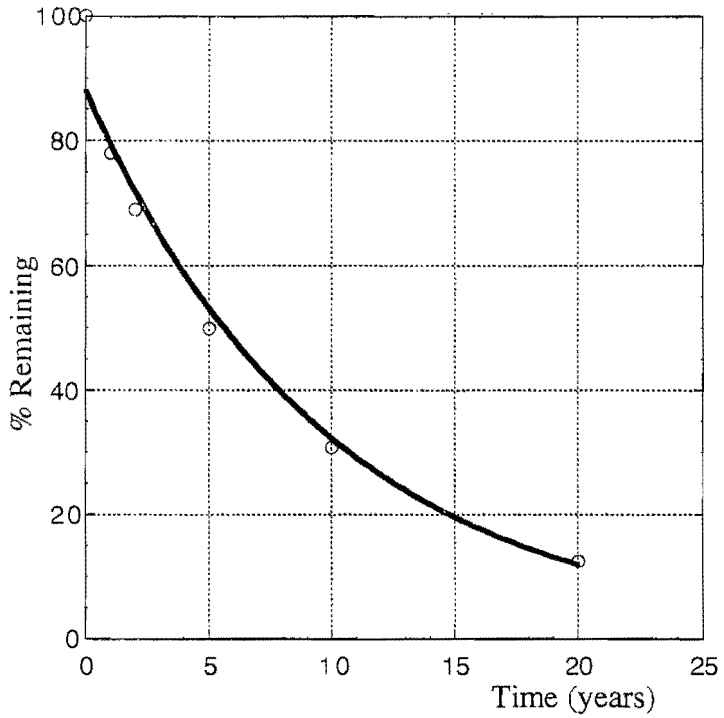

%remaining = 88*e^(-0.1*years)

R = 0.99

Figure 4.3.4_2 Time dependence of TCA removal from the mesa after catastrophic drum failure.

4.4 Future work

A new grid that will extend an additional 152 m (500 ft.) to both the north and west is being developed. We will examine boundary effects with this new grid to assure that the results of our best-fit scenario are not overly affected by the zero-concentration boundary conditions. We have also created a high resolution grid of the site with six embedded well bores. We plan to use the high resolution grid to allow modeling of active and passive venting, as well as to explore remediation and closure options.

5.0 - CONCLUSIONS

The site numerical model is calibrated using the pore-gas data gathered at MDA L. The model demonstrates that diffusive behavior captures the general characteristics of the vapor plume. The base-case diffusion coefficient of $4x10^{-6}$ m^2/s fits the data better than either $1x10^{-6}$ or $8x10^{-6}$ m^2/s. A goodness-if-fit analysis is used to determine the model that best fits the data. The best-fit simulation maintains a zero concentration boundary in the subsurface basalt unit and along the northern and western boundary of the model. Also, no liquid source is used, in agreement with field observations.

The observed site data and simulated results indicate that the vapor plume is currently at a near steady condition, both in size and in concentration. The constant flushing of the plume at the mesa sides and in the deep basalt should maintain the plume at its current size until the liquid source, which remains in buried drums, has been exhausted. Therefore, we do not expect that the vapor plume will spread any closer to White Rock or to the deep aquifer than its current location. Also, because no migration of liquid is thought to occur, we do not expect that VOCs can travel as liquids to the deep aquifer either. Estimates based on a conservative TCA source predict that the plume will start to shrink when the source is depleted, before the year 2060.

The site numerical model also shows that the asphalt cover at MDA L acts as a non-diffusive barrier that forces VOCs to migrate downward and laterally to reach pathways to the atmosphere. Little or no flux emanates from the asphalt itself, but enhanced flux from the mesa top to the atmosphere occurs around the edges of the asphalt. This predicted behavior agrees qualitatively with the surface flux measurements also gathered at the site. In the future, the site model will provide a useful tool for exploring the effects of potential corrective measures, such as venting and/or removing the asphalt cover at MDA L.

The agreement of the numerical model with the pore-gas and surface flux data indicates that the monitoring program has successfully defined both the nature and extent of the vapor plume at MDA L. The simulations show that both current and future plume growth (over the next 50 years) are quite small. These results, combined with the recent observations of slowly changing pore-gas concentrations, indicate that pore-gas monitoring could be performed less frequently than the current three-month interval. Yearly monitoring should be sufficient to capture any changes in the plume. In fact, the simulation of catastrophic drum failure predicts that the results of such an event would be apparent in the monitoring data for several years. Therefore, yearly monitoring is

not only capable of capturing the current rate of plume growth, it should also be capable of detecting a large perturbation, such as a drum burst.

6.0 - ACKNOWLEDGEMENTS

This work was supported by the LANL Environmental Restoration Project for the U.S. Department of Energy. The authors would like to thank Veraun Chipman for his help with data visualization. We would also like to thank David Rogers, Bryan Travis, Diana Hollis, and Dennis Newell for their reviews of this manuscript.

7.0 - REFERENCES

Birdsell, K.H., W.E. Soll, K.M. Bower, A.V. Wolfsberg, T. Orr, T.A. Cherry, (1997). "Simulations of Groundwater Flow and Radionuclide Transport in the Vadose and Saturated Zones Beneath Area G, Los Alamos National Laboratory," Los Alamos National Laboratory manuscript LA-13299-MS.

Bishop, C.W., (1991). "Hydrologic Properties of Vesicular Basalt," Masters thesis, University of Arizona.

Boas, M.L. (1983), Mathematical Methods in the Physical Sciences, Wiley, New York.

Freeze, R.A., Cherry, J.A. (1979), Groundwater, Prentice-Hall, NJ, USA.

Fetter, C.W. (1999), "Contaminant Hydrogeology", Prentice-Hall, NJ, USA.

Fuentes, H.R., W.L. Polzer, and J. L. Smith, (1991). "Laboratory Measurements of Diffusion Coefficients for Trichloroethylene and Orthoxylene in Undisturbed Tuff", J. Environ. Quality, 20, p. 215-221.

Gardner, J.N., F. Goff, S. Garcia and R.C. Hagan (1986). "Stratigraphic Relations and Lithologic Variations in the Jemez Volcanic Field, New Mexico," J. of Geophysical Research 91, 1763-1778.

George, Denise (1997). Unstructured Toolbox for Modeling and Simulation, LA-UR-97-3052, presented at the 1997 Workshop on Computational Electronics and Nanoelectronics, Urbana, Illinois, October 20-22, 1997.

Griggs, R.L. (1955). Geology and Groundwater Resources of the Los Alamos Area, New Mexico, U.S. Geologic Survey Report to the U.S. Atomic Energy Commission.

Krier, D., P. Longmire, R. Gilkeson and H.J. Turin, (1997). "Geologic, Geohydrologic, and Geochemical Data Summary of MDA G, Technical Area 54, Los Alamos National Laboratory," Los Alamos National Laboratory document LA-UR-95-2696.

LANL (1999). "Material Disposal Areas Core Document," Los Alamos National Laboratory draft report LA-UR-99-4423.

LANL (2000). "RFI Report for Material Disposal Areas G, H, and L at Technical Area 54," Los Alamos National Laboratory report LA-UR-00-1140.

Lyon, B.F., Holmes, J.A., Kosiewicz, S.T., Wilbert, K.A., Travis, C.C. (1996). Estimation of corrosion on carbon steel TRU waste drums using Poisson distribution, J. Hazardous Materials, 51, p. 165-179.

Meisher and Anderson (1994)., Ambient monitoring of Volatile Organic Compounds at Los Alamos National Laboratory in TA54, Areas G and L, LANL doc. 63525.

Neeper, D.A. (1997). "Monitoring Pore Gas Pressure and Chemical Constituents at Wells 54-1015 and 54-1016 during 1995 and 1996," SEA-SF-TR-97-170.

Purtymun, W.D., (1995). "Geologic and Hydrologic Records of Observation Wells, Test Holes, Test Wells, Supply Wells, Springs, and Surface Water Stations in the Los Alamos Area," Los Alamos National Laboratory manuscript LA-12883-MS.

Rogers, D.B., (2000). "Conceptual Model for Vapor Movement at MDAs," Los Alamos National Laboratory document LA-UR-00-950.

Rogers, D.B., and B.M. Gallaher, (1995). "The Unsaturated Hydraulic Characteristics of the Bandelier Tuff," Los Alamos National Laboratory manuscript LA-12968-MS.

Smith, R.L. and Bailey, R.A. (1966). "The Bandelier Tuff: A Study of Ash-Flow Eruption Cycles and Zoned Magma Chambers," Bulletin of Volcanology 29, 83-104.

Smith, J., Hardesty, B., McCranie, N. (1999a), Quarterly Pore Gas Sampling at TA-54 MDA L and MDA G First Quarter FY1999, PMC-LA-99-002.

Smith, J., Hardesty, B., McCranie, N. (1999b), Quarterly Pore Gas Sampling at TA-54 MDA L and MDA G Second Quarter FY1999, PMC-LA-99-003.

Smith, J., Crocker, J., McCranie, N. (1998), Quarterly Pore Gas Sampling at TA-54 MDA L and MDA G Second Quarter FY1998, PMC-LA-98-009.

Turin, H.J., (1995). "Subsurface Transport Beneath MDA G: A Conceptual Model," Los Alamos National Laboratory document LA-UR-95-1663.

Trease, H., George D., Gable C. W., J. Fowler, A. Kuprat, A. Khamyaseh (1996), The X3D Grid Generation System Numerical Grid Generation in Computational Fluid Dynamics and Related Fields, B. K. Soni, J. F. Thompson, H. Hausser and P. R. Eiseman, Engineering Research Center, Mississippi State Univ. Press.

Trent, B., (1992), "Analysis of the Pore Gas Monitoring at Area L, TA-54 Los Alamos National Laboratory," Los Alamos National Laboratory document.

Trujillo, V., Gilkeson, R., Morgenstern, M., Kreir, D. (1998), Measurements of Surface Emission Flux Rates for Volatile Organic Compounds at TA-54, LA-13329

van Genuchten, M.T., (1980). "A Closed-Form Equation for Predicting the Hydraulic Conductivity of Unsaturated Soils," Soil Science Society of America Journal 44, 892-898

Vaniman, D., G. Cole, J. Gardner, J. Conaway, D. Broxton, S. Reneau, M. Rice, G. WoldeGabriel, J. Blossom, and F. Goff, (1998). "Development of a Site-Wide Geologic Model for Los Alamos National Laboratory," Los Alamos National Laboratory unpublished document.

Zyvoloski, G.A., B.A. Robinson, Z.V. Dash, and L.L. Trease, (1997). "Summary of the Models and Methods for the FEHM Application - A Finite Element Heat- and Mass-Transfer Code," Los Alamos National Laboratory manuscript LA-13307-MS.